Integration of Grid Fins for the Optimal Design of Missile Systems

by

Timothy Wayne Ledlow II

A thesis submitted to the Graduate Faculty of
Auburn University
in partial fulfillment of the
requirements for the Degree of
Master of Science

Auburn, Alabama
August 2, 2014

Keywords: grid fins, optimization, missile design

Approved by

Roy Hartfield, Chair, Walt and Virginia Waltosz Professor of Aerospace Engineering
John Burkhalter, Professor Emeritus of Aerospace Engineering
Andrew Shelton, Assistant Professor of Aerospace Engineering

Abstract

Grid fins are unconventional missile control and stabilization devices that produce unique aerodynamic characteristics that are vastly different from that of the conventional planar fin. History has shown that grid fins are able to achieve much higher angles of attack than planar fins without experiencing any effects of stall. They are also able to produce much lower hinge moments than planar fins, which allows for the use of smaller actuators for fin control. However, the major drawback of grid fins that has prevented them from seeing more applications in missile control is the high drag that is associated with the lattice structure, which is substantially larger than that of a comparable planar fin. Despite the high drag produced by grid fins, there are still several applications where the grid fin is an ideal candidate for missile control. One such application is the maximization of the target strike capability of a missile that is released from an airplane at a designated altitude. The goal of this work is to integrate a set of grid fin aerodynamic prediction algorithms into a missile system preliminary design code in an effort to maximize the target strike area of a missile using both planar fins and grid fins as aerodynamic control devices. It was found that a missile system using grid fins for aerodynamic control is able to strike a larger target area with a higher degree of accuracy than a similar missile system using equivalent planar fins for aerodynamic control.

Acknowledgments

The author would like to thank Dr. Roy Hartfield for providing the opportunity, encouragement, and support for conducting this research. Special thanks are also due to Dr. John Burkhalter for providing his assistance and expertise regarding grid fins and the missile trajectory optimization program, as well as allowing the use of his subsonic and supersonic grid fin prediction programs. The author would also like to thank his parents for their years of support and encouragement, without which none of this would be possible.

Table of Contents

List of Figures

List of Tables

Nomenclature

α	Angle of Attack
β	Compressibility Factor
ΔC_p	Differential Pressure Coefficient
δ	Fin Incidence Angle
δ_{th}	Displacement Thickness of Boundary Layer
Γ	Vortex Strength
γ	Specific Heat Ratio
λ	Fin Leading Edge Sweep Angle
μ	Mach Angle
ϕ	Roll Angle
ρ	Density
ρ_{al}	Density of Aluminum
A	Area
A^*	Throat Area
$A_{\delta_{th}}$	Reduction in Fin Capture Area
A_{ref}	Reference Area
B_2	Fin Span from Body Centerline

C	Chord Length
C_A	Axial Force Coefficient
C_N	Normal Force Coefficient
C_S	Side Force Coefficient
$C_{M_{mc}}$	Pitching Moment Coefficient about Moment Center
C_{Ni}	Imaged Normal Force Coefficient
C_{Si}	Imaged Side Force Coefficient
CF	Transonic Correction Factor
D_B	Diameter of the Missile Body
D_{ref}	Reference Length
ft	Feet
H	Height of Grid Fin
H_B	Height of Grid Fin Support Structure
I_{yy}	Mass Moment of Inertia About the Y Axis
$ibase$	Number of Cells in Fin Base Corner
$in.$	Inches
$itip$	Number of Cells in Fin Tip Corner
$L_{p_{tot}}$	Total Length of the Grid Fin Panels
M	Mach Number
m_{GF}	Mass of a Single Grid Fin

mph	Miles per Hour
n_{dy}	Number of Cells in Horizontal Direction
n_{dz}	Number of Cells in Vertical Direction
np	Number of Fin Element Intersection Points
p	Pressure
R_B	Radius of the Missile Body
Re	Reynolds Number
S_{abi}	Span-wise Length of the Imaged Panel
S_{ab}	Span-wise Length of the Actual Panel
T_{HT}	Distance from Nose of Body to Tail Location
T_{XCG}	Distance from Nose of Body to Center of Gravity Location
thk	Average Fin Element Thickness
$ttle$	Total Length of the Grid Fin Elements in the Plane Perpendicular to the Freestream
X_L	Length of Missile Body
X_{LN}	Length of the Nose

Chapter 1

Introduction

The grid fin (also known as a lattice control surface) is an unconventional aerodynamic control device that consists of an outer frame which supports an inner lattice of intersecting planar surfaces of small chord length. Unlike the conventional planar fin, the grid fin is positioned perpendicular to the freestream direction, which allows the oncoming flow to pass through the inner lattice structure. This design provides unique aerodynamic performance characteristics that are vastly different from that of the planar fin. Extensive research has been performed on grid fins since their development in the 1970s in an effort to better understand these unique aerodynamic performance characteristics. This research has included wind tunnel testing of different grid fin configurations [1–5], Computational Fluid Dynamics (CFD) analysis [6–8], and the development of different theoretical formulations for the prediction of grid fin aerodynamics [9–14].

The U.S. Army Aviation and Missile Command in particular has performed extensive research on various grid fin configurations [1–4], including a suite of grid fin performance prediction codes that was developed for the U.S. Army Aviation and Missile Command by Burkhalter in the mid 1990s [9–11]. Different theoretical formulations were used for the subsonic, transonic, and supersonic flow regimes due to the drastically different flow fields that the grid fin experiences in each Mach regime. These codes use a vortex lattice approach in the subsonic and transonic flow regimes, with a correction factor that is applied in the transonic flow regime to account for mass flow spillage due to the choking of the flow within each individual cell of the grid fin. The formulation for the supersonic flow regime uses a modified version of Evvard's Theory to determine the differential pressure coefficient for each panel of the grid fin. The results produced by these theoretical formulations have

been compared with experimental data obtained from wind tunnel test results of different grid fin geometries at various Mach numbers, incidence angles, and roll angles. It has been determined that these theoretical formulations are able to accurately and efficiently predict the aerodynamics of a wide range of grid fin geometries, and is a suitable tool for application in the preliminary design analysis of missile systems.

The purpose of this work is to incorporate the grid fin aerodynamic prediction capability that was developed by Burkhalter into an existing preliminary design analysis tool that has been developed at Auburn University for the optimal design of missile systems. This program uses an aerodynamic prediction tool known as AERODSN to predict the aerodynamic characteristics of typical missile configurations in flight. AERODSN was developed by Sanders and Washington for the U.S. Army Missile Command in 1982 to provide an efficient and reliable tool to predict the aerodynamics for a typical cylindrical missile body configuration with wings or planar tail fins or both [15]. AERODSN has proven to be an effective aerodynamic prediction tool, and has been successfully applied to a multitude of aerospace design problems [16–19].

Optimization is a very important tool that provides the ability to find good solutions for highly complex problems where the best solution is not readily apparent and cannot be solved for directly. There are several different optimization schemes that can be used to intelligently search a given solution space for global optimal solutions. The missile system preliminary design tool used in this work has four different optimization schemes incorporated in the code that have been successfully applied to aerospace design problems in the past [16–22]. These optimization schemes include a modified ant colony optimizer, a particle swarm optimizer, a binary-encoded genetic algorithm, and a real-encoded genetic algorithm. The modified ant colony optimization scheme was selected for use in this work due to its proven effectiveness at solving complex aerospace design problems. It has been shown that the modified ant colony has the ability to be more effective than many established optimization methods, as

it is able to converge more quickly and find better solutions than competing optimization algorithms [20, 21].

The incorporation of the grid fin aerodynamics into AERODSN allowed for a preliminary analysis that compared the performance of planar fins versus grid fins as the aerodynamic control device for an unpowered missile system. The modified ant colony optimization scheme was used to find the optimal planar fin and grid fin designs for a given missile configuration that maximized the target strike area for an unpowered missile dropped from an airplane flying with a horizontal velocity of 492.8 ft/sec at an altitude of 23,000 ft.

Chapter 2

Background: Grid Fins

Grid fins were initially developed in the 1970s by the Soviet Union. The first flow field analysis of grid fins was performed by Russian researchers, who were able to provide a basic understanding of the unique aerodynamics associated with the grid fin [23]. Grid fins can be used as either an aerodynamic stabilizer or a control surface for a missile or munition configuration. The unconventional geometry of the grid fin is what really separates it from the conventional planar fin. Planar fins can generally be characterized by four geometrical parameters: root chord, tip chord, span, and thickness. The grid fin, however, adds an extra dimension, requiring five geometrical parameters: element thickness, cell spacing, span, height, and chord length [2]. Figure 2.1 below shows a comparison between an example of a general missile configuration with grid fins (2.1a) versus an example of a general missile configuration with planar fins (2.1b).

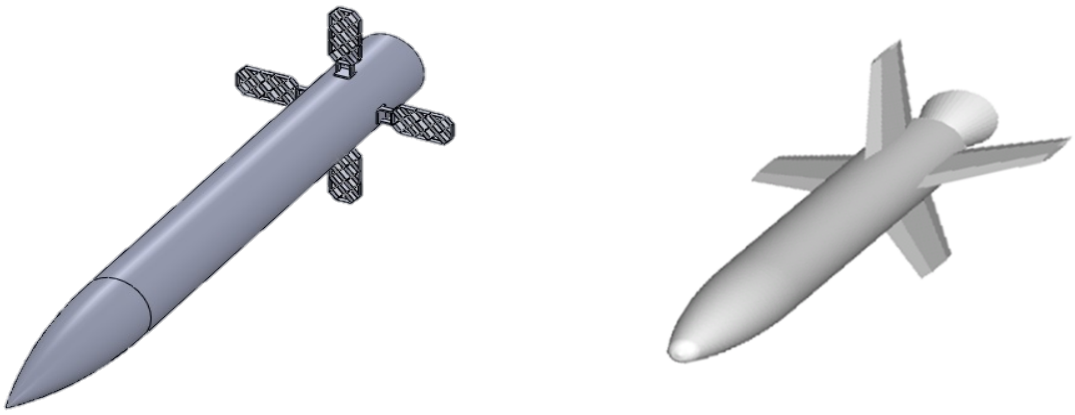

(a) Missile Configuration with Grid Fins (b) Missile Configuration with Planar Fins

Figure 2.1: Comparison of Grid Fins vs. Planar Fins

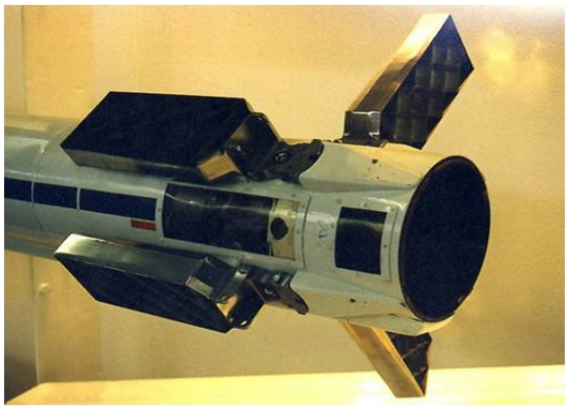

(a) Foldable for Compact Storage [24]

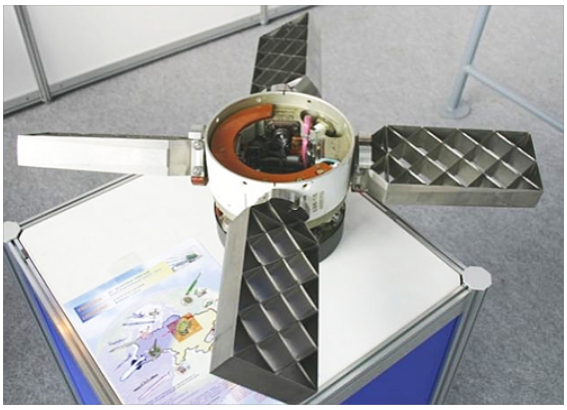

(b) Generate Low Hinge Moments [25]

Figure 2.2: Grid Fin Features

There are several distinct advantages to using grid fins as an aerodynamic stabilizer or as a control surface instead of planar fins:

1) Grid fins are able to be folded down against the body of the missile for compact storage (Figure 2.2a), which can be particularly helpful when there are size limitations for the missile, such as if it is a tube-launched device.

2) Grid fins generate much lower hinge moments than planar fins (Figure 2.2b), and are therefore able to use smaller actuators for fin deflection than their planar fin counterparts would require [8].

3) The multiple cell arrangement of the grid fin makes it less prone to stall at higher angles of attack than the traditional planar fin. A typical grid fin can reach angles of attack near 40 - 50 degrees before experiencing any loss in lift, as seen by the wind tunnel test results of a single grid fin in Mach 0.35 flow in Figure 2.3.

4) The truss structure of the grid fin is inherently strong, which allows the lattice walls to be extremely thin, thus reducing the weight of the fin.

5) Grid fins provide greater control effectiveness in the supersonic flight regime than a comparable planar fin [2].

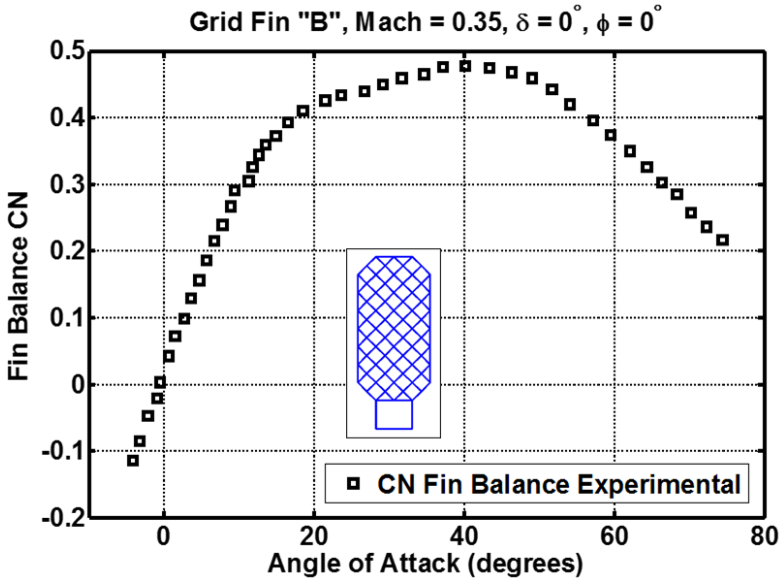

Figure 2.3: Wind Tunnel Results Showing the High Angle of Attack Capability of Grid Fins (Mach 0.35 Flow) [2]

6) A grid fin that is mounted in the vertical position will still produce a normal force at any finite body angle of attack, which is a unique characteristic compared to any other lifting surface system that is currently in use on missile systems [10].

There are also several disadvantages to the use of grid fins as an aerodynamic stabilizer or as a control surface:

1) Grid fins produce higher drag than planar fins, especially in the transonic flight regime.

2) Grid fins perform very poorly in the transonic flight regime due to the choking of the flow within the individual grid fin cells and the shocks that are present in the flow field.

3) Grid fins have a high manufacturing cost due to their complex geometry [8].

The large amount of drag that is produced by the grid fin is undesirable in most applications. There have been several different efforts that have been conducted in an effort to reduce the drag of the grid fin [4, 8]. Miller and Washington found that it is possible to considerably lower the drag of a grid fin without resulting in a major impact on other aerodynamic properties by adjusting the cross-section shape of each panel within the lattice

(a) American Massive Ordnance Penetrator (MOP) [26]

(b) Russian Vympel R-77 [25]

Figure 2.4: Examples of Uses of Grid Fins

structure [4]. Each advantage and disadvantage of the grid fin concept must be thoroughly analyzed within the constraints of the given problem before a definitive decision can be made on their use [1].

Since their inception in the 1970s, grid fins have found rather limited use compared to their planar fin counterparts. The majority of the application of grid fins has been on Russian ballistic missile designs such as the SS-12, SS-20, SS-21, SS-23, and the SS-25. Grid fins have also been used on some launch vehicle designs, most notably as emergency drag brakes on the launch escape system for the Russian Soyuz spacecraft [24]. Grid fins have also found use on conventional bombs such as the American Massive Ordnance Penetrator (Figure 2.4a), and the Russian Vympel R-77 (Figure 2.4b). Another recent application of grid fins is the Quick Material Express Delivery System (Quick-MEDS), which is a precision-guided supply pod that is designed to deliver small, critically needed packages from Unmanned Aircraft Systems (UAS) in the air to troops on the ground [27].

Chapter 3

Theoretical Analysis

A set of robust theoretical analysis tools capable of quickly predicting the aerodynamic coefficients associated with a cruciform grid fin configuration on a missile body was developed for the U.S. Army Aviation and Missile Command by Burkhalter in the mid 1990s [9–11]. Separate theoretical formulations were developed for the different Mach regimes in order to correctly capture the flow structure of the grid fin for any given flight condition.

Table 3.1 gives a brief description of the assumed flow structure for a grid fin for each Mach regime. For a freestream Mach number $M < 0.8$, the flow is assumed to be compressible subsonic flow, and a vortex lattice solution is used to calculate the loading on each individual element of the grid fin [9]. In the transonic regime ($0.8 < M < 1.0$), the flow is assumed to choke within each individual cell of the grid structure, resulting in mass flow spillage around the edges of the grid fin. A correction factor is applied to the normal force coefficient to account for this effect in the theoretical analysis. A bow shock is formed in front of the grid fin in the low supersonic Mach regime ($1.0 < M < 1.4$), resulting in compressible subsonic flow behind the shock. A schematic showing the bow shock in front of the grid fin can be seen in Figure 3.1. This is treated as transonic flow, with a correction factor once again

Table 3.1: Assumed Grid Fin Flow Structure in Different Mach Number Regimes

Mach Number	**Flow Regime**	**Assumed Flow Structure**
$M < 0.8$	Subsonic	Compressible, subsonic flow
$0.8 < M < 1.0$	Transonic	Choked flow within grid structure
$1.0 < M < 1.4$	Transonic	Bow shock in front of grid fin, subsonic flow behind shock
$1.4 < M < 1.9$	Supersonic	Shock attachment and reflection
$M > 1.9$	Supersonic	Unreflected shocks

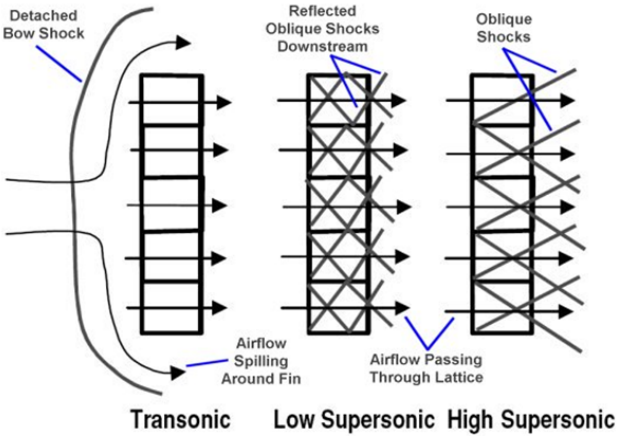

Figure 3.1: Different Possible Shock Structures for a Grid Fin [24]

being applied to the normal force coefficient to account for the mass flow spillage. This bow shock is "swallowed" by the grid fin at higher supersonic Mach numbers ($1.4 < M < 1.9$), leading to the formation of attached oblique shocks that are reflected within the grid fin structure (Figure 3.1). At higher supersonic Mach numbers ($M > 1.9$), the flow structure for the grid fin is assumed to consist of attached, unreflected oblique shocks (Figure 3.1). A modified version of Evvard's Theory is used to determine the loading produced by the grid fin in the supersonic Mach regime.

The grid fin aerodynamic prediction algorithms as developed by Burkhalter consisted of two standalone programs, one for the subsonic flow regime and the other for the supersonic flow regime. Each program contained a modified form of slender body theory that was combined with Jorgensen's theory for the prediction of the body alone aerodynamic coefficients [10]. The integration of the grid fin aerodynamic prediction programs into AERODSN required the combination of the subsonic and supersonic prediction programs as well as the removal of the body alone aerodynamic coefficient prediction method. Another modification that was required for the integration of the grid fin aerodynamics into AERODSN was the addition of the normal shock equations to account for the effects of the bow shock that forms in front of the grid fin in the low supersonic Mach regime ($1.0 < M < 1.4$). This addition

allowed for the grid fin aerodynamic prediction algorithms to be successfully used for any Mach number ranging from approximately Mach 0.1 up to Mach 3.5.

3.1 Subsonic Grid Fin Analysis

3.1.1 Linear Analysis: Subsonic

A vortex lattice solution was used as the linear subsonic formulation for predicting the loading on each individual element of the grid fin lattice structure. A horseshoe vortex is placed on each individual element of the grid fin, as illustrated in Figure 3.2. This vortex is defined using ten node points. Points 1 and 6 are placed at the quarter chord location of the grid fin element, while points 2 and 7 are located at the trailing edge of the element. The remaining points define the vortex trailing legs, which extend aft of the panel in the direction of the freestream flow [9]. A control point and a unit normal vector are then placed at the three quarter chord location of the panel. A boundary condition that requires the flow at the control point location of a panel to be tangent to the surface of that panel is then applied so that the strength of each vortex within the lattice structure can be determined. The velocity at each control point is composed of three different components: the freestream velocity, the cross-flow velocity (body up-wash term), and the induced velocity that takes into account the vortex strengths of the surrounding vortices [9].

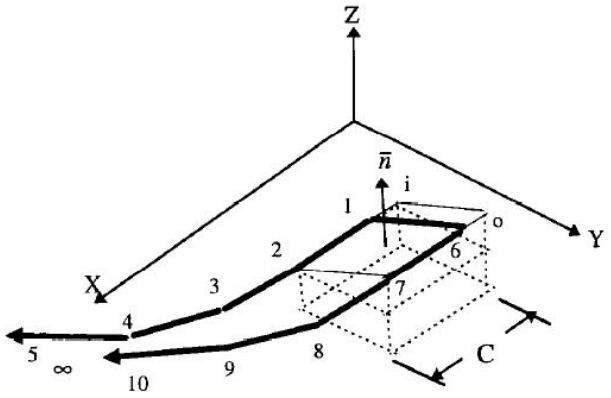

Figure 3.2: Vortex Lattice on a Single Grid Fin Panel [9]

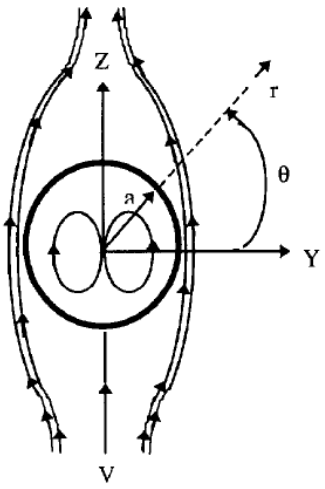

Figure 3.3: Resulting Flowfield from a Freestream Doublet [9]

The cross-flow velocity term is determined using a potential flow solution of an infinite doublet in the freestream, an illustration of which can be seen in Figure 3.3. The induced velocity from the doublet and freestream can be written in vector form as:

$$\overline{V}_0 = V_\infty cos\left(\alpha\right)\hat{\imath} + \left(-V_\theta sin\left(\theta\right) + V_r cos\left(\theta\right)\right)\hat{\jmath} + \left(V_\theta cos\left(\theta\right) + V_r sin\left(\theta\right) + V_\infty sin\left(\alpha\right)\right)\hat{k} \quad (3.1)$$

The compressible form of the Biot-Savart law gives the velocity induced by a vortex filament segment at a control point [9]:

$$\overline{v}_\Gamma = -\frac{\Gamma\beta^2}{4\pi}\int\frac{\overline{r}x d\bar{l}}{|r_\beta|^3} \quad (3.2)$$

where β is the compressibility factor:

$$\beta = \sqrt{1 - M^2} \quad (3.3)$$

The dot product of the velocity vector from Equation 3.1 and the unit normal for a panel gives the velocity component normal to the surface of the panel. This component of velocity must be equal to zero in order to satisfy the flow tangency boundary condition mentioned previously. The application of this boundary condition results in the following

expression:

$$\overline{v}_\Gamma \cdot \overline{n} = \left[\left(-\frac{\beta^2}{4\pi} \int \frac{\overline{r} x d\overline{l}}{|r_\beta|^3} \right)_x \cdot n_x + \left(-\frac{\beta^2}{4\pi} \int \frac{\overline{r} x d\overline{l}}{|r_\beta|^3} \right)_y \cdot n_y + \left(-\frac{\beta^2}{4\pi} \int \frac{\overline{r} x d\overline{l}}{|r_\beta|^3} \right)_z \cdot n_z \right] \cdot \Gamma = B \quad (3.4)$$

which can be rearranged to solve for the unknown vortex filament strength Γ, where the "A" matrix is the inverse of the bracketed term from Equation 3.4 and the "B" matrix is the known velocities induced at the panel control point by the freestream doublet combination [9]:

$$[\Gamma] = [A]^{-1} \cdot [B] \quad (3.5)$$

An iterative procedure is used to find the vortex strengths in order to avoid taking the inverse of a large "A" matrix [28], and is as follows. First, the vortex strengths associated with the first fin are found as if there are no other fins present in the flow. Second, the vortex strengths for the second fin are found as if fins 1 and 2 are the only fins present in the flow, and the vortex strengths of fin 1 are known. This process continues in a similar fashion for the remaining two grid fins, each time including the known strengths from the previous fins [28]. Once the vortex strengths of the fourth and final fin are known, the entire process is repeated for several iterations until there is no significant difference in vortex strength values from one iteration to the next. It has been found that a large number of iterations is not necessary to achieve accurate results, and therefore a total of six iterations are used in this work.

Once the iterative process is complete and the vortex strengths for all four grid fins are known, the Kutta-Joukowski theorem is used to compute the aerodynamic loads on each individual element of each grid fin:

$$C_{\hat{F}} = \frac{2 * \Gamma * S}{S_{ref}} \quad (3.6)$$

where S is the slant length of the individual grid fin element that is being analyzed. This force coefficient can then be turned into different components by multiplying by the unit normal vector for that grid fin element:

$$C_{\hat{N}} = C_{\hat{F}} \cdot \overline{n}_z \tag{3.7}$$

$$C_{\hat{S}} = C_{\hat{F}} \cdot \overline{n}_y \tag{3.8}$$

$$C_{\hat{A}} = C_{\hat{F}} \cdot \overline{n}_x \tag{3.9}$$

The total axial force for the grid fin is assumed to consist of four different components: induced drag, skin friction drag, pressure drag, and interference drag from the fin element intersection points [9]. The induced drag is the drag produced due to fin deflection angle, and is given by:

$$C_{Ai} = C_N tan(\delta) \tag{3.10}$$

The skin friction drag is determined by calculating the wetted area of the fin and converting it to a flat plate area with an assumed laminar or turbulent boundary layer, as a function of Reynolds number. The drag contribution due to pressure is a function of the frontal area of the grid fin and the local dynamic pressure [9]:

$$C_{Adp} = \frac{S_{wetf} t}{2 * S_{ref} C} \tag{3.11}$$

An empirical formulation that was derived using experimental data is used to determine the interference drag due to the fin element intersection points:

$$C_{Axp} = 2 * 0.000547 * (np + 2) \tag{3.12}$$

where $(np + 2)$ is the total number of fin intersection points, including the base support structure. The total grid fin axial force coefficient is simply the sum of these four contributions:

$$C_{Ax} = C_{Axi} + C_{Axf} + C_{Axdp} + C_{Axp} \tag{3.13}$$

It was observed that the fin axial force changes very little with angle of attack, and is therefore assumed to be independent of angle of attack [9].

3.1.2 Nonlinear Analysis: Subsonic

Unlike planar fins, the linear aerodynamics region of the grid fin begins to break down at an angle of attack around 5° to 8°, resulting in the need for a nonlinear theoretical formulation to more accurately model the aerodynamic coefficients. Experimental results obtained through wind tunnel testing of different grid fin geometries were used to develop a semi-empirical formulation for the nonlinear aerodynamic region at higher angles of attack:

$$C_N = \left[\left(\frac{C_{N\delta} sin(\delta)}{1 + k_2 \left(\frac{B_g}{H}\right)^2 \left(\frac{C}{H}\right) sin^2(\delta)} \right) * \left(k_6 - \frac{\left(k_3 - k_4 \sqrt{\frac{B_g}{H}}\right) C_{N\alpha} sin(\alpha)}{1 + k_5 \left(\frac{B_g}{H}\right)^2 \alpha^2} \right) + \left(\frac{C_{N\alpha} sin(\alpha)}{1 + k_1 \left(\frac{B_g}{H}\right)^2 \left(\frac{C}{H}\right) sin^2(\alpha)} \right) \right] cos^2(2\alpha - \delta) \tag{3.14}$$

This subsonic semi-empirical formulation uses the initial lift-curve slope from the linear vortex lattice theory and also attempts to incorporate the influence from the major grid fin geometric properties, such as the fin span to height ratio (B_g/H) and the fin chord length to height ratio (C/H). A more in-depth analysis of the nonlinear aerodynamics of grid fins can be found in Reference [12].

3.2 Transonic Grid Fin Analysis

Grid fins exhibit unique aerodynamic characteristics in the transonic flight regime compared to the traditional planar fin. Planar fins experience their maximum normal force coefficients in the transonic region, while grid fins experience what is known as a "transonic bucket". An illustration of the transonic bucket can be seen in Figure 3.4. This phenomenon is a result of the choking of the individual cells of the grid fin, which causes mass flow spillage around the edges of the grid fin. In order to capture this characteristic, the grid fin aerodynamic prediction tool applies a correction factor to the normal force coefficient when operating in the transonic flow regime.

The first step to calculating the correction factor is to determine the thickness of the boundary layer within the cells of the grid fin. Blasius' theorem is used to calculate the displacement thickness of the boundary layer:

$$\delta_{th} = \frac{1.7208 * C}{\sqrt{Re_c}} \tag{3.15}$$

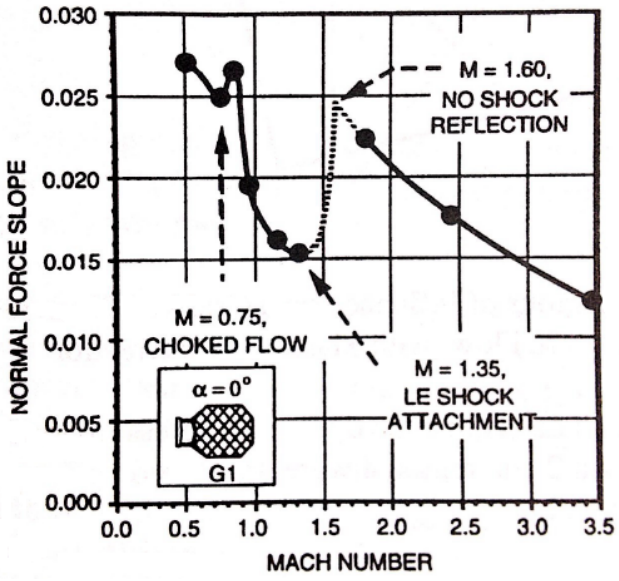

Figure 3.4: Grid Fin Normal Force Coefficient Transonic Bucket [1]

The presence of the boundary layer results in an area reduction within the individual grid fin cells, which can be determined by:

$$A_{\delta_{th}} = 2 * \delta_{th} + thk * ttle \tag{3.16}$$

The area required to choke the flow at the given Mach number is then determined using the following isentropic relationship:

$$A^* = \frac{A_{cap} * M}{\left[\frac{2\left(1+\frac{\gamma-1}{2}M^2\right)}{\gamma+1}\right]^{\left(\frac{\gamma+1}{2(\gamma-1)}\right)}} \tag{3.17}$$

If the calculated exit area is less than or equal to the value calculated using Equation 3.17, the flow is considered to be choked and a correction factor is then determined by calculating the reduction in mass flow rate between the choked and unchoked conditions:

$$CF = \frac{A_{ex} * \sqrt{\gamma P_0 \rho_0 \left(\frac{2}{\gamma+1}\right)^{\left(\frac{\gamma+1}{\gamma-1}\right)}}}{A_{cap}\rho_\infty V_\infty} \tag{3.18}$$

which is then applied as a multiplier to the calculated fin forces and moments, thus capturing the reduction in grid fin performance in the transonic flow regime.

For any transonic Mach number above Mach 1.0 (Table 3.1), a normal shock is assumed to be present in front of the fin, which results in a subsonic flow-field behind the shock. The well-known normal shock equations (found in Reference [29]) are used to determine the resulting Mach number and freestream pressure behind the shock:

$$M_2^2 = \frac{1 + \left[\frac{\gamma-1}{2}\right] M_1^2}{\gamma M_1^2 - \frac{\gamma-1}{2}} \tag{3.19}$$

$$\frac{p_2}{p_1} = 1 + \frac{2\gamma}{\gamma+1}\left(M_1^2 - 1\right) \tag{3.20}$$

The subsonic theoretical formulation is then used to determine the loads on the grid fins, including the transonic correction factor if the flow within the cells of the grid fin is determined to be choked.

3.3 Supersonic Grid Fin Analysis

3.3.1 Linear Analysis: Supersonic

A modified version of Evvard's theory is used as the linear supersonic theoretical formulation in the grid fin aerodynamic prediction tool. The original version of Evvard's theory determines the differential pressure coefficient distribution over a swept wing with a supersonic leading edge [30]. Figure 3.5 shows an illustration of the original version of Evvard's theory, showing the various supersonic regions associated with a typical planar fin.

Similar to the subsonic formulation, the supersonic formulation is applied to the grid fin on a panel by panel basis, resulting in the need for a modified version of Evvard's theory that takes account of end-plate effects. These end-plate effects are a result of the unique lattice structure of the grid fin, and are not accounted for in the original form of Evvard's theory. Figure 3.6 shows the two possible cases for the flow over the individual grid fin elements: without crossing Mach lines (Figure 3.6a) and with crossing Mach lines (Figure 3.6b).

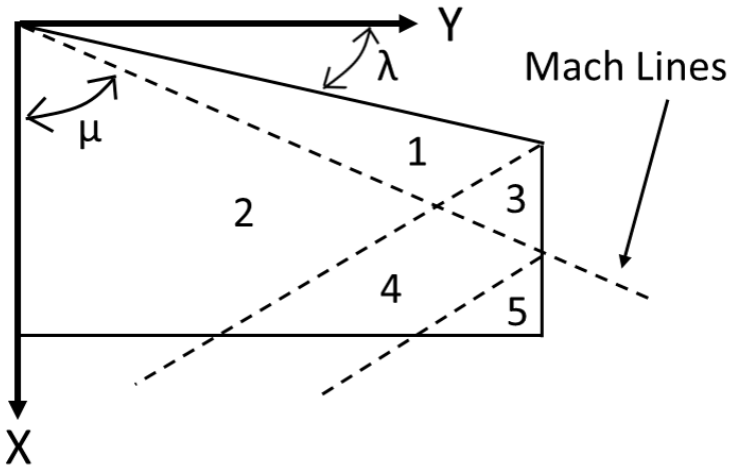

Figure 3.5: Classical Evvard's Theory [9]

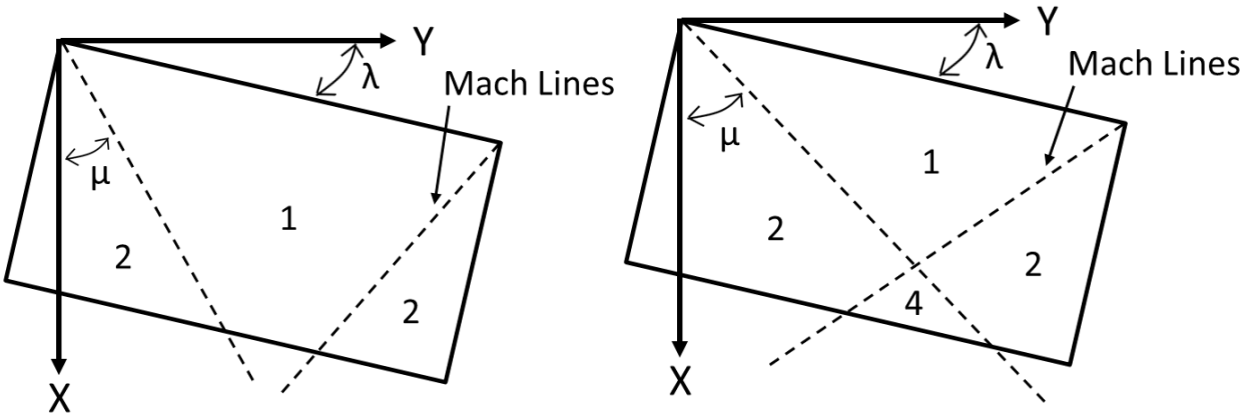

(a) Without Crossing Mach Lines (b) With Crossing Mach Lines

Figure 3.6: Modified Evvard's Theory [9]

It can be seen in Figure 3.6 that only the differential pressure calculations for regions 1, 2, and 4 are required for the determination of the loading on a grid fin element. The differential pressure coefficients for each region were derived by Evvard and can be seen by the following equations:

$$[\Delta C_p]_1 = \frac{4\alpha}{\sqrt{B^2 - tan^2(\lambda)}} \tag{3.21}$$

$$[\Delta C_p]_2 = \frac{1}{\pi}[\Delta C_p]_1 \left[cos^{-1}\left(\frac{x * tan(\lambda) - B^2 y}{B\left(x + y * tan(\lambda)\right)}\right) + cos^{-1}\left(\frac{x * tan(\lambda) - B^2 y}{B\left(x - y * tan(\lambda)\right)}\right)\right] \tag{3.22}$$

$$[\Delta C_p]_4 = [\Delta C_p]_2 - \frac{1}{\pi}[\Delta C_p]_1 \left[-cos^{-1}\left(\frac{x_a + y_a\left(2B + tan(\lambda)\right)}{x_a + y_a tan(\lambda)}\right)\right] \tag{3.23}$$

where

$$B^2 = M^2 - 1 \tag{3.24}$$

The orientation of the grid fin is extremely important in the supersonic theoretical formulation, as that is what dictates the size of the different pressure regions on the grid fin panels. Each element of the grid fin must be oriented at some dihedral angle θ, pitched at some deflection angle δ, rolled to some angle ϕ, and finally pitched to some angle of attack α [11]. The grid fin elements are terminated at each end by end plates that are not

necessarily perpendicular to the lifting surface, making it very important to understand the geometric angles involved with each element lifting surface. Once each point of each element of the grid fin has been pitched and rolled to its final position, the leading edge sweep and the effective angle of attack can be determined. This process is described in further detail in References [11] and [31].

Once the differential pressure coefficients for the different regions on the grid fin element are known, the aerodynamic coefficients for normal force, side force, and axial force can be determined by subdividing the element into a series of small rectangles with area "A" [9]. The loading for each subelement can be seen by:

$$\Delta C_N = \frac{\Delta C_p * A * U_{NZ}}{S_{ref}} \tag{3.25}$$

$$\Delta C_S = \frac{\Delta C_p * A * U_{NY}}{S_{ref}} \tag{3.26}$$

$$\Delta C_A = \frac{\Delta C_p * A * U_{NX}}{S_{ref}} \tag{3.27}$$

The total force coefficients for the grid fin can then be found by simply summing the loading on each individual subelement. The total fin axial force coefficient is calculated using the same component contributions as those that are described for the subsonic theoretical formulation.

3.3.2 Nonlinear Analysis: Supersonic

Similar to the linear subsonic grid fin aerodynamic formulation, the linear supersonic grid fin aerodynamic formulation is only accurate for low angles of attack, and typically begins to break down at angles of attack around 5 ° to 8 °. A semi-empirical formulation for the supersonic nonlinear aerodynamic region at higher angles of attack can be seen as:

$$C_N = \left.\frac{\delta C_{N\delta}}{1+\frac{\delta}{\delta_{max}}}\right|_{\alpha=0} + \left.\frac{\alpha C_{N\alpha}}{1+\frac{\alpha}{\alpha_{max}}}\right|_{\delta=0} * \left(1 - \left.\frac{\delta C_{N\delta}}{1+\left(\frac{\delta}{\delta_{max}}\right)^2}\right|_{\alpha=0}\right) \tag{3.28}$$

where $C_{N\alpha}$ and $C_{N\delta}$ are the initial lift-curve slopes with respect to angle of attack and fin deflection, respectively, that are calculated from the modified Evvard's theory. A more in-depth discussion of the development of this formulation can be found in Reference [31].

3.4 Fins in the Vertical Position

As was mentioned previously, grid fins possess a unique characteristic that no other lifting surface system that is currently in use on missile systems possesses, as they are able to produce a normal force at any finite body angle of attack when mounted in the vertical position [10]. The normal force coefficient for a grid fin in the vertical position (either the top or bottom of the missile body) is still found in the same manner as discussed in the previous sections, but the values of $C_{N\delta}$ and $C_{N\alpha}$ are considerably smaller than those for the fins in the horizontal position [11, 28]. The lift-curve slopes for a fin in the vertical position are still determined via the vortex lattice theory (subsonic) or Evvard's theory (supersonic), although an error is introduced that is not present in the linear analysis.

This error arises due to the streamline flow near the top and bottom of the body surface and from the body vortices emanating from the nose of the missile [11]. The grid fins on the top and bottom of the missile body do not experience oncoming flow that is the same as the freestream direction, and are therefore assumed to be immersed in a stream tube that is nearly parallel to the body [11]. Burkhalter determined from an analysis of available experimental data that the average angle of attack of the top and bottom fin due to body alteration of the incident streamlines should be assumed to be approximately $\alpha/2$ [28].

3.5 Fin-Body Carry-Over Loads

In traditional airplane design, the effects of the wing-body carry-over loads can be accounted for by viewing the aerodynamic characteristics as being dominated by the wing such that no body is present in the flow [32]. This traditional assumption is valid for cases where the wing span is large compared to the body diameter, but a different approach is required

in the case of very small wings in comparison to the body diameter, as is characteristic of many missile designs [32].

The fin-body carry-over loads are modeled in the grid fin aerodynamic prediction tool through an imaging scheme in which each panel element is imaged inside the missile body, as illustrated by Figure 3.7. The basic assumption is that each imaged element inside the body carries the same load per unit span as its corresponding element outside the body [10]. The geometry of the imaged element is defined by imaging the endpoints of the "real" panel outside the body along radial lines to the center of the body, using the following equations:

$$y_a = \frac{y_1 R_B^2}{r_a^2} \qquad z_a = \frac{z_1 R_B^2}{r_a^2} \tag{3.29}$$

$$y_b = \frac{y_2 R_B^2}{r_b^2} \qquad z_b = \frac{z_2 R_B^2}{r_b^2} \tag{3.30}$$

The chord length of the imaged element is assumed to be the same as that of the corresponding "real" panel. The normal force coefficients and side force coefficients due to carry-over loads are both determined by this method, while the axial force coefficients are not imaged [10]. The equations for the determination of the imaged normal force coefficient and the imaged side force coefficient can be seen by:

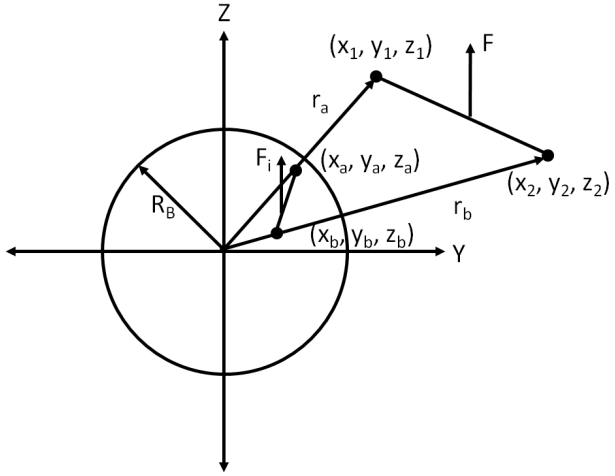

Figure 3.7: Imaging Scheme for Fin-Body Carry-Over Load Calculation [9]

$$C_{Ni} = C_N \left(\frac{S_{abi}}{S_{ab}} \right) \tag{3.31}$$

$$C_{Si} = C_S \left(\frac{S_{abi}}{S_{ab}} \right) \tag{3.32}$$

where S_{ab} and S_{abi} are the span-wise lengths of the "real" and imaged panels, respectively. These values are determined by:

$$S_{ab} = \sqrt{(y_1 - y_2)^2 + (z_1 - z_2)^2} \tag{3.33}$$

$$S_{abi} = \sqrt{(y_a - y_b)^2 + (z_a - z_b)^2} \tag{3.34}$$

This imaging technique is used to predict the fin-body carry-over loads for each theoretical formulation described in this section.

Chapter 4

Validation of Grid Fin Prediction Algorithm

The validation of the subsonic, transonic, and supersonic grid fin aerodynamic theoretical formulations was performed by conducting several tests using three different grid fin designs (as seen in Figure 4.1) for multiple Mach numbers, fin incidence angles, and configuration roll angles. The theoretical results obtained from the grid fin prediction algorithm were compared with experimental wind tunnel data that was extracted from References [1, 2, 4, 9–11]. Experimental data was available for two general cases: four grid fins mounted on a cylindrical missile body in a cruciform configuration (allowing for the capture of the fin-body carry-over loads), and a single grid fin mounted on a fin balance (eliminating the fin-body carry-over loads).

The missile body that was used for these wind tunnel tests consisted of a 15 *in.* tangent ogive nose section followed by a 37 *in.* cylindrical main body section [2]. Table 4.1 shows the

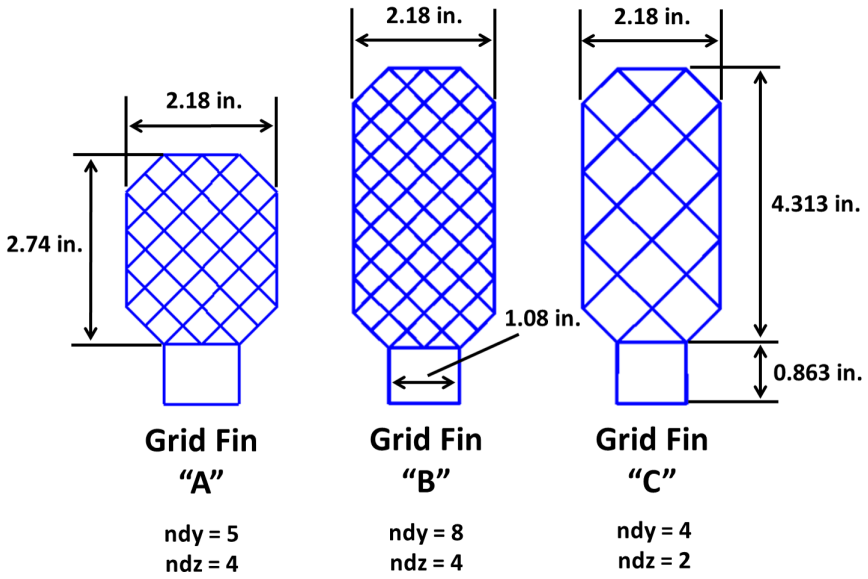

Figure 4.1: Grid Fin Geometries Used for Validation

Table 4.1: Missile Body Configuration Parameter Values

X_{LN}	15 $in.$
T_{XCG}	26 $in.$
T_{HT}	46 $in.$
X_L	52 $in.$
R_B	2.5 $in.$
A_{ref}	19.63 $in.^2$
D_{ref}	5 $in.$

values for the missile body configuration parameters in inches, which are defined in Figure 4.2. A consistent reference length ($D_{ref} = 5\ in.$) and reference area ($A_{ref} = 19.63\ in.^2$) was used for all experimental test data. The values of the reference length and reference area correspond to the missile base diameter and the missile base area, respectively.

The three grid fin geometries that were analyzed for this validation effort can be seen in Figure 4.1. The same base support structure is used for each grid fin, as well as the same chord length (0.384 $in.$). The average element thickness of the inner lattice structure is 0.008 $in.$ and the average element thickness of the outer support elements is 0.03 $in.$ for each grid fin design.

The validation results presented in Figures 4.4 - 4.7 in the following pages represent the normal force coefficient, axial force coefficient, and pitching moment coefficient versus angle

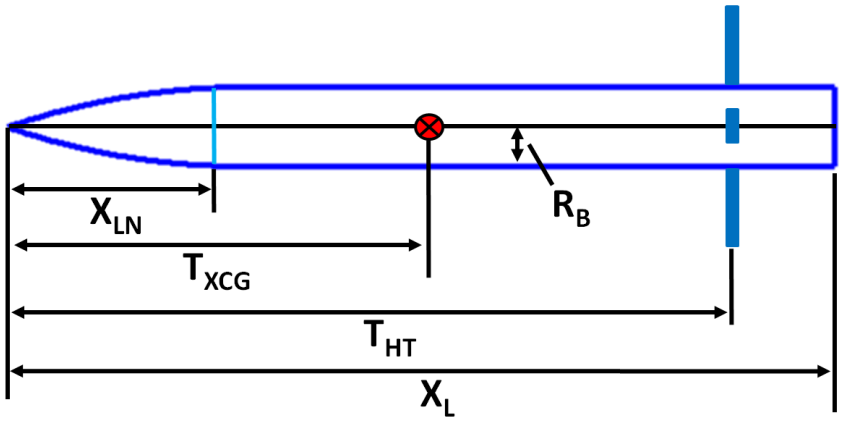

Figure 4.2: Parameters Defining Missile Geometry [12]

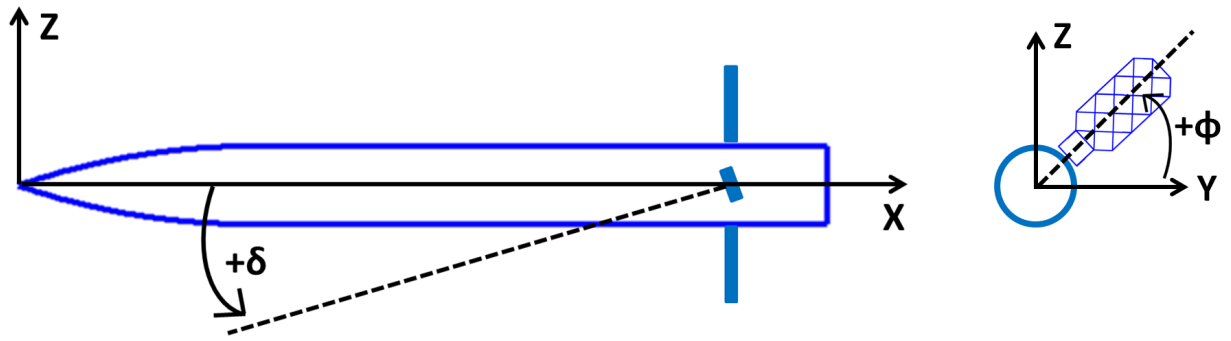

Figure 4.3: Sign Convention for Orientation Angles [9]

of attack for four grid fins mounted on a missile body in a cruciform configuration. The fin-body carry-over loads are included in the results in each of these plots. Figures 4.8 - 4.10 show the normal force coefficient and axial force coefficient (when available) for a single grid fin, allowing for a comparison of theoretical and experimental data without the inclusion of fin-body carry-over loads.

Figure 4.4 shows C_N, C_A, and $C_{M_{mc}}$ for grid fin "A" mounted in a cruciform configuration at Mach numbers ranging from 0.5 to 0.9. The grid fins are at an incidence angle of $0\,^\circ$ and a roll angle of $0\,^\circ$. The theoretical results were found to closely match the wind tunnel data overall, with slight discrepancies at high angles of attack. It is clear that the correction for the transonic effects is accurate for this particular configuration, as the theoretical data matches the experimental data very well in both the Mach 0.8 case and the Mach 0.9 case.

Figure 4.5 shows C_N, C_A, and $C_{M_{mc}}$ for grid fin "A" in a cruciform configuration at Mach 0.5 at different fin incidence angles (ranging from $\delta = 0\,^\circ$ to $\delta = 20\,^\circ$) and different roll angles ($0\,^\circ$ and $45\,^\circ$ roll angles). The fin orientation sign convention is defined in Figure 4.3. It can be seen that the theoretical results have excellent agreement with the experimental data for these cases. The theoretical model was able to accurately predict the aerodynamic coefficients for each fin deflection case as well as the roll case for this particular configuration. It should also be noted that the aerodynamic coefficients are symmetric about $\alpha = 0\,^\circ$ for all cases where there is no fin deflection, and is not symmetric about $\alpha = 0\,^\circ$ in the cases with fin deflection, as would be expected.

Figure 4.6 shows C_N, C_A, and $C_{M_{mc}}$ for grid fin "B" in a cruciform configuration at Mach 0.7 at several different roll angles, ranging from $0\,^\circ$ to $67.5\,^\circ$. It can be seen that the theory matches the experimental results well in the low angle of attack region, but tends to under-predict the normal force coefficient and the pitching moment coefficient at high angles of attack.

Figure 4.7 shows C_N, C_A, and $C_{M_{mc}}$ for grid fin "A" in a cruciform configuration at Mach 2.51 at several different fin incidence angles, ranging from $0\,^\circ$ to $20\,^\circ$. It can be seen that Evvard's theory provides an accurate match in the linear aerodynamics region, but the nonlinear theoretical model tends to over-predict the normal force coefficient and pitching moment coefficient at high angles of attack.

Figure 4.8 shows the fin balance normal force coefficient and axial force coefficient for grid fin "B" at various Mach numbers and roll angles. It can be seen that the theoretical grid fin formulation provides good agreement with experimental data in the single grid fin case. A comparison of Figures 4.6a and 4.8c and Figures 4.6e and 4.8d show that the imaging scheme for the fin-body carry-over loads is accurately predicting the aerodynamics associated with the fin-body interaction.

Figure 4.9 shows several different subsonic fin balance cases, including varying the fin deflection angle. A comparison of the normal force coefficient for grid fin "A" at Mach 0.5 both with and without fin-body carry-over loads (Figures 4.5 and 4.9, respectively) show that the imaging scheme is once again able to accurately capture the effects of the fin-body interactions.

Figure 4.10 shows several supersonic fin balance cases, including the low supersonic cases where there is a normal shock in front of the grid fin. It can be seen that the theoretical formulations are able to match the aerodynamic characteristics of the grid fin very well in each of these cases for a wide range of angles of attack.

It can be concluded from this comparison of theoretical versus wind tunnel test results that the grid fin aerodynamic prediction algorithms are suitable for use as a preliminary

design tool for missile systems. The grid fin prediction algorithms were able to match the aerodynamic characteristics of three different grid fin geometries for a wide range of Mach numbers ranging from Mach 0.25 to Mach 3.5, for several different fin incidence angles and configuration roll angles. It was shown that both the subsonic and supersonic linear aerodynamic theoretical models are able to provide very good matches with the initial lift curve slope, and that the nonlinear semi-empirical formulations are sufficient for preliminary-level engineering design analysis. It was also shown that the imaging scheme used to capture the fin-body carry-over loads for the grid fins is able to accurately capture the effects of the interaction between the grid fins and the missile body.

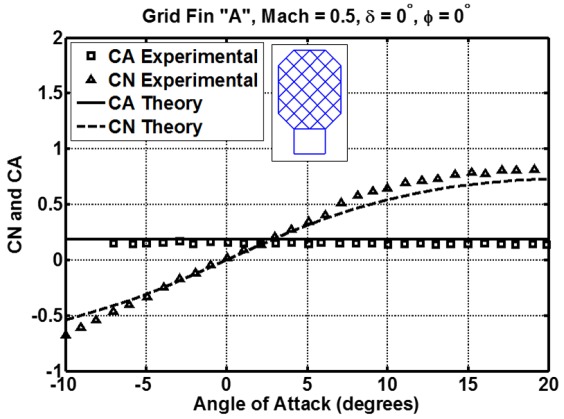

(a) Grid Fin "A", Mach 0.5, C_N and C_A

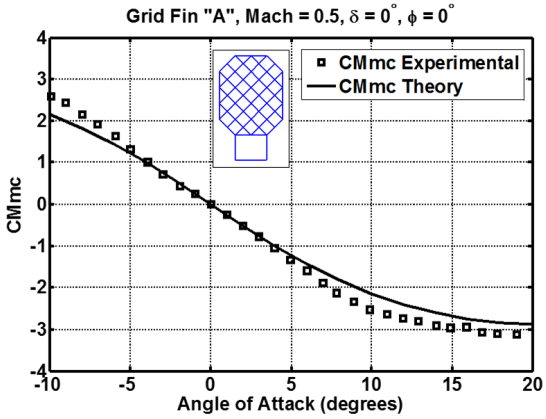

(b) Grid Fin "A", Mach 0.5, $C_{M_{mc}}$

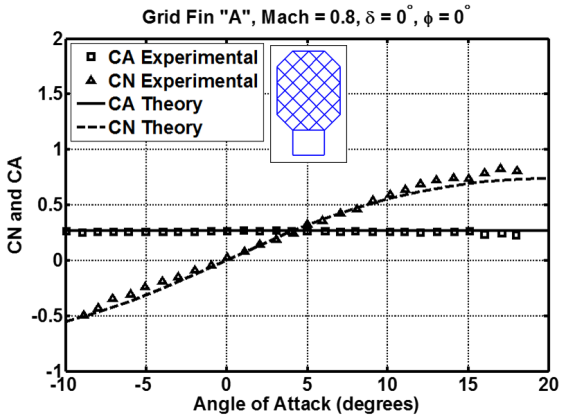

(c) Grid Fin "A", Mach 0.8, C_N and C_A

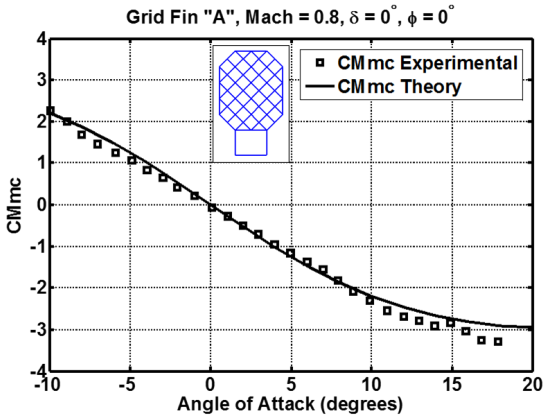

(d) Grid Fin "A", Mach 0.8, $C_{M_{mc}}$

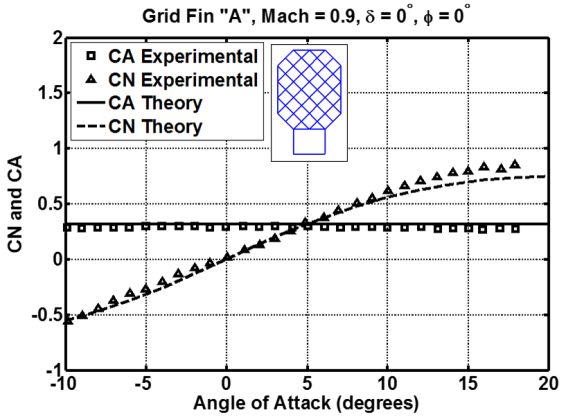

(e) Grid Fin "A", Mach 0.9, C_N and C_A

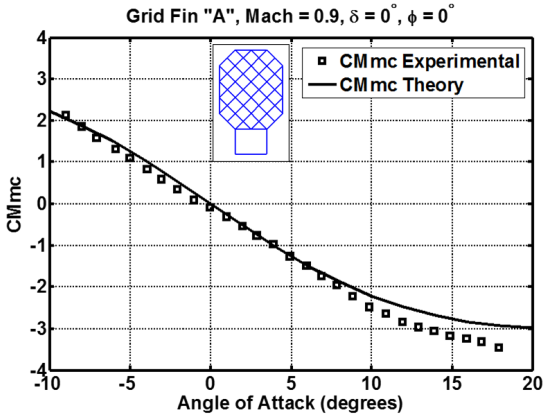

(f) Grid Fin "A", Mach 0.9, $C_{M_{mc}}$

Figure 4.4: Subsonic Mach Numbers, Including Fin-Body Carry-Over Loads

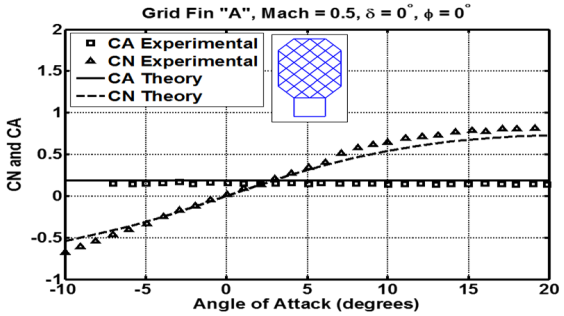

(a) Grid Fin "A", 0° Incidence Angle, C_N and C_A

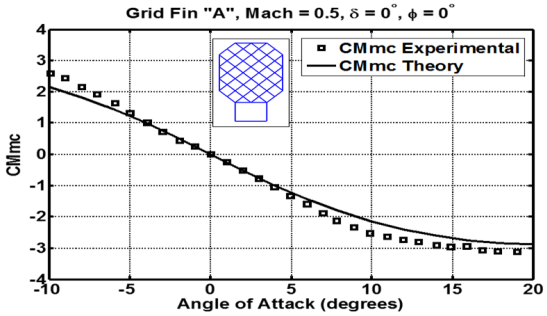

(b) Grid Fin "A", 0° Incidence Angle, $C_{M_{mc}}$

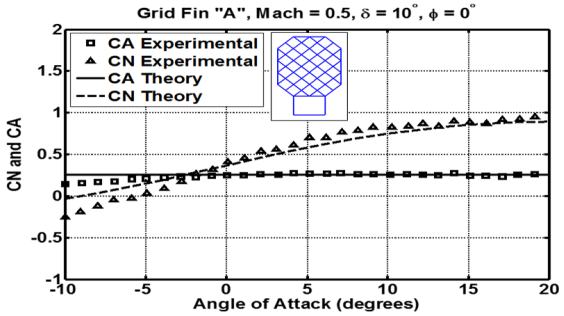

(c) Grid Fin "A", 10° Incidence Angle, C_N and C_A

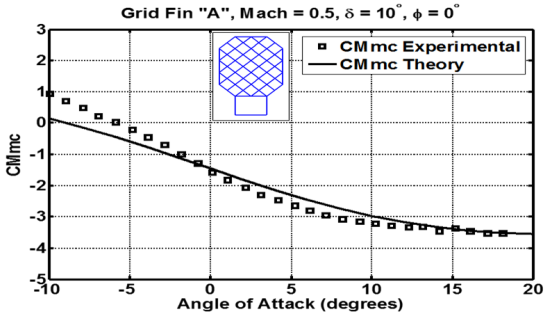

(d) Grid Fin "A", 10° Incidence Angle, $C_{M_{mc}}$

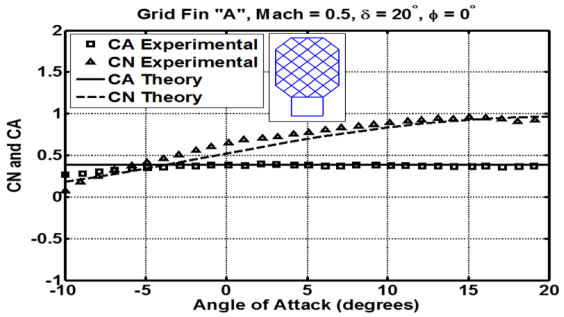

(e) Grid Fin "A", 20° Incidence Angle, C_N and C_A

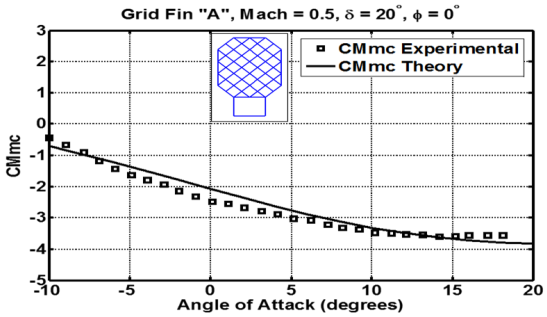

(f) Grid Fin "A", 20° Incidence Angle, $C_{M_{mc}}$

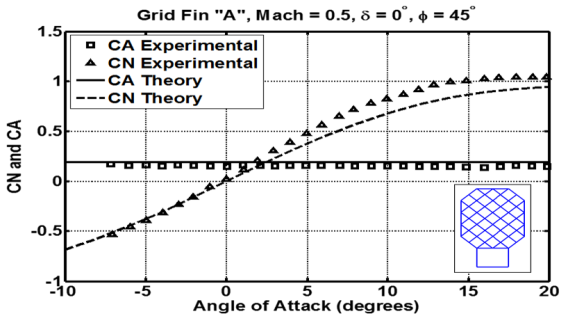

(g) Grid Fin "A", 45° Roll Angle, C_N and C_A

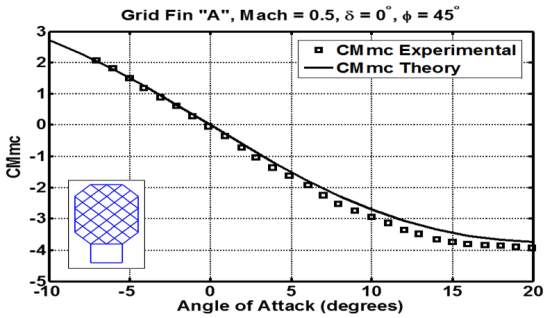

(h) Grid Fin "A", 45° Roll Angle, $C_{M_{mc}}$

Figure 4.5: Varying Incidence and Roll Angles at Mach 0.5, Including Fin-Body Carry-Over Loads

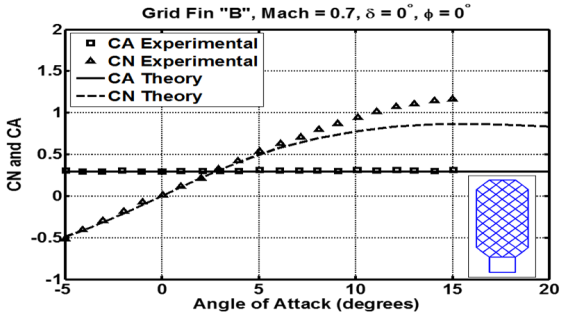

(a) Grid Fin "B", 0° Roll Angle, C_N and C_A

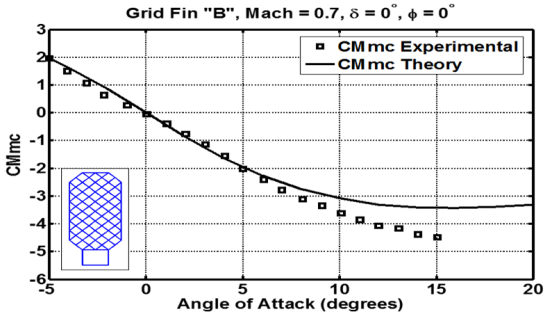

(b) Grid Fin "B", 0° Roll Angle, $C_{M_{mc}}$

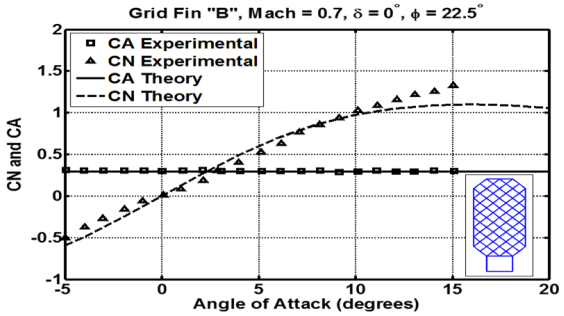

(c) Grid Fin "B", 22.5° Roll Angle, C_N and C_A

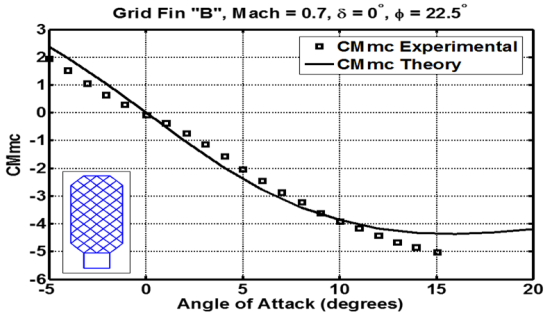

(d) Grid Fin "B", 22.5° Roll Angle, $C_{M_{mc}}$

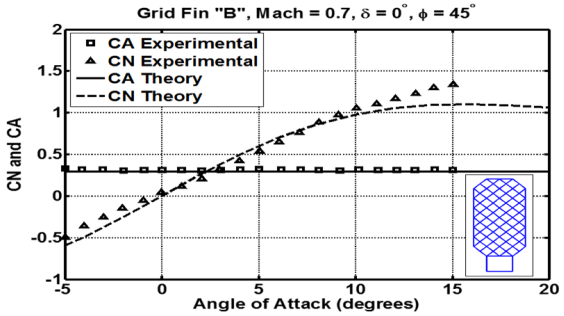

(e) Grid Fin "B", 45° Roll Angle, C_N and C_A

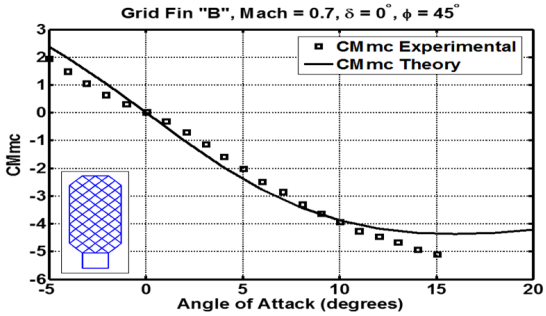

(f) Grid Fin "B", 45° Roll Angle, $C_{M_{mc}}$

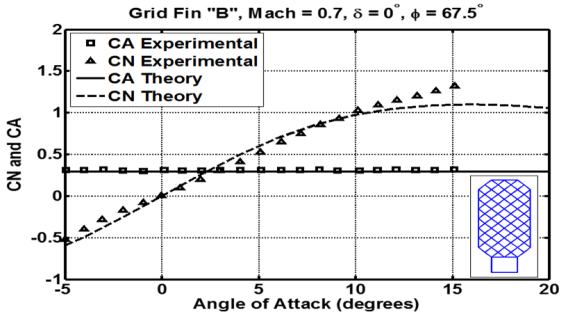

(g) Grid Fin "B", 67.5° Roll Angle, C_N and C_A

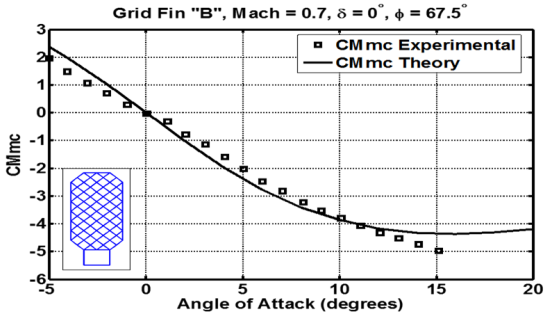

(h) Grid Fin "B", 67.5° Roll Angle, $C_{M_{mc}}$

Figure 4.6: Varying Roll Angle at Mach 0.7, Including Fin-Body Carry-Over Loads

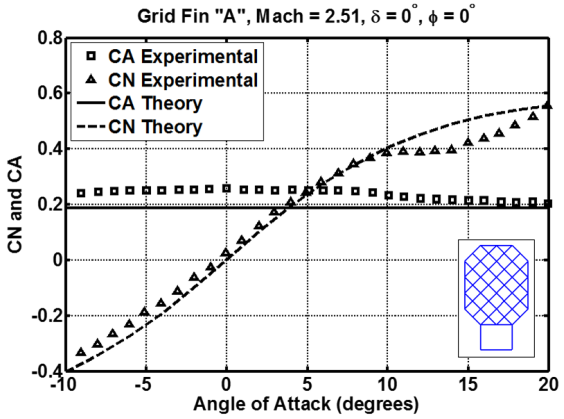

(a) Grid Fin "A", 0° Incidence Angle, C_N and C_A

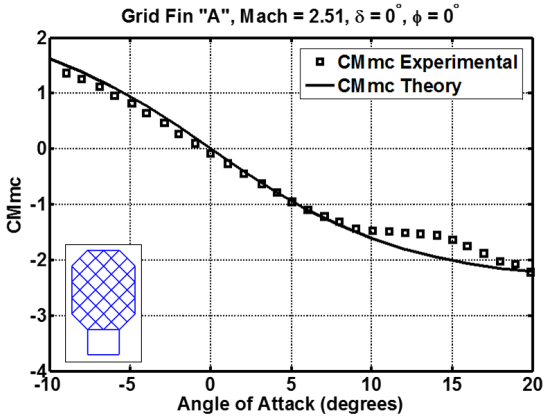

(b) Grid Fin "A", 0° Incidence Angle, $C_{M_{mc}}$

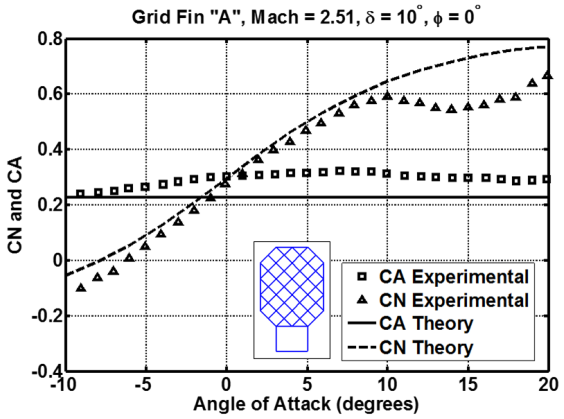

(c) Grid Fin "A", 10° Incidence Angle, C_N and C_A

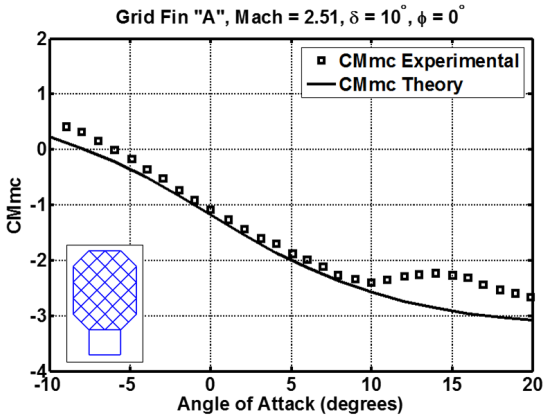

(d) Grid Fin "A", 10° Incidence Angle, $C_{M_{mc}}$

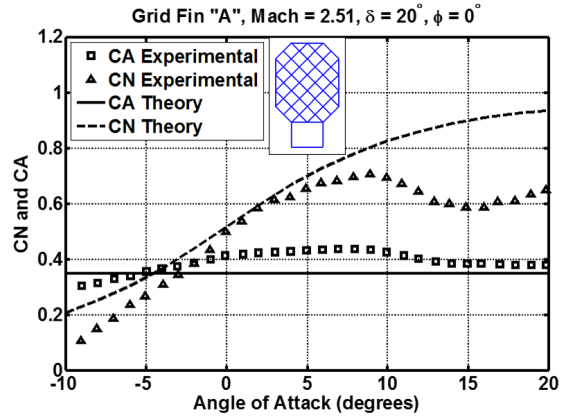

(e) Grid Fin "A", 20° Incidence Angle, C_N and C_A

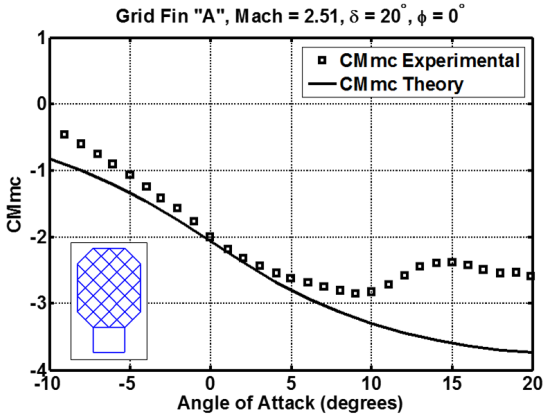

(f) Grid Fin "A", 20° Incidence Angle, $C_{M_{mc}}$

Figure 4.7: Varying Incidence Angle at Mach 2.51, Including Fin-Body Carry-Over Loads

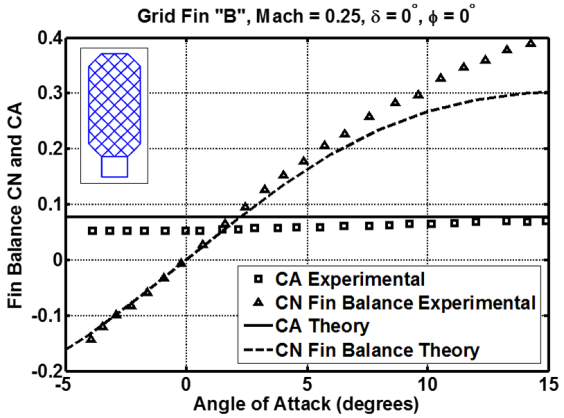

(a) Grid Fin "B", Mach 0.25, 0 ° Roll Angle

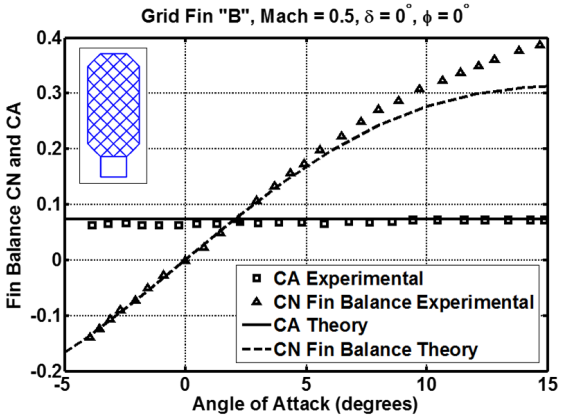

(b) Grid Fin "B", Mach 0.5, 0 ° Roll Angle

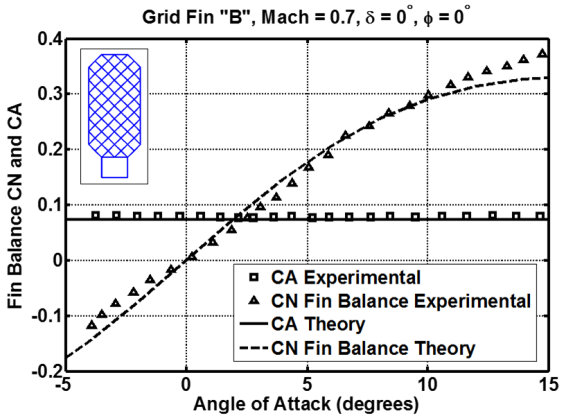

(c) Grid Fin "B", Mach 0.7, 0 ° Roll Angle

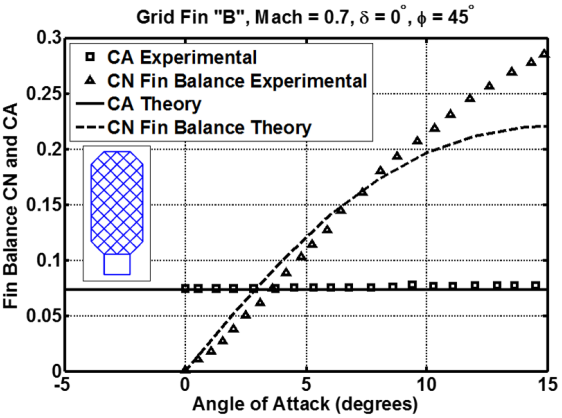

(d) Grid Fin "B", Mach 0.7, 45 ° Roll Angle

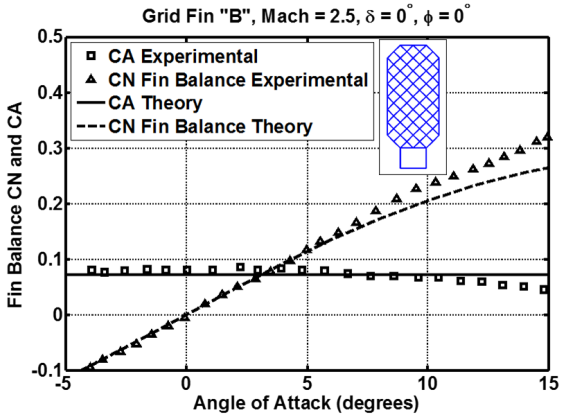

(e) Grid Fin "B", Mach 2.5, 0 ° Roll Angle

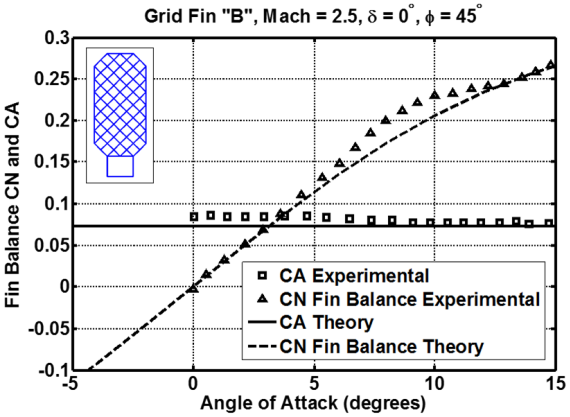

(f) Grid Fin "B", Mach 2.5, 45 ° Roll Angle

Figure 4.8: Single Grid Fin, Not Including Fin-Body Carry-Over Loads

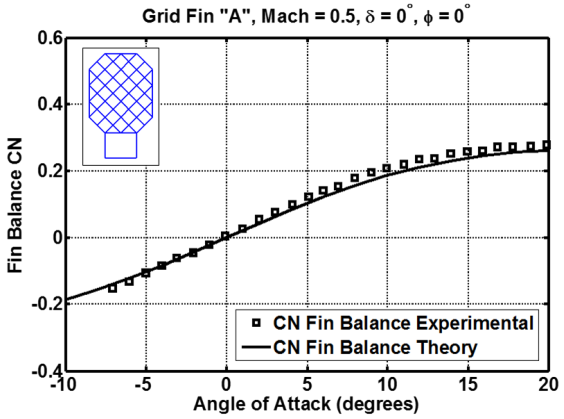

(a) Grid Fin "A", Mach 0.5, 0° Incidence Angle

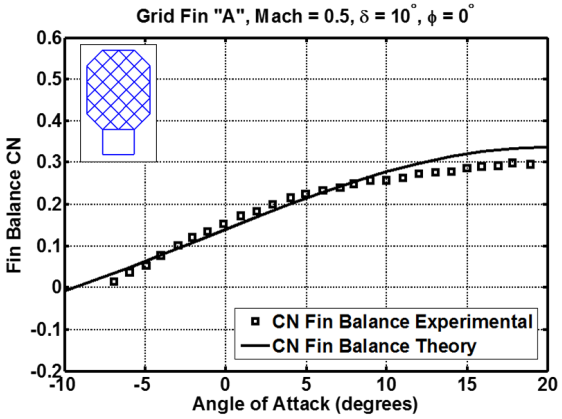

(b) Grid Fin "A", Mach 0.5, 10° Incidence Angle

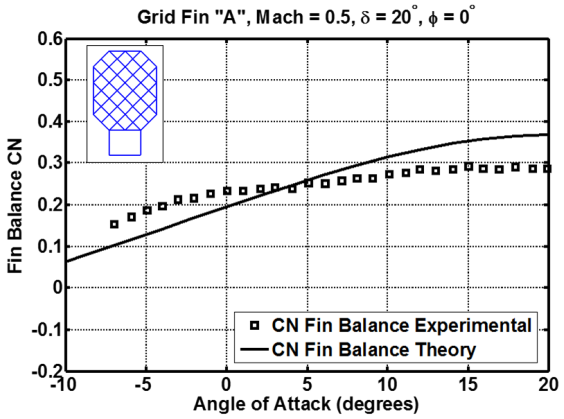

(c) Grid Fin "A", Mach 0.5, 20° Incidence Angle

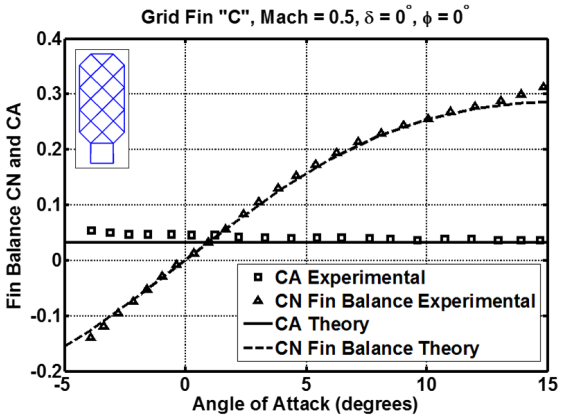

(d) Grid Fin "C", Mach 0.5, 0° Incidence Angle

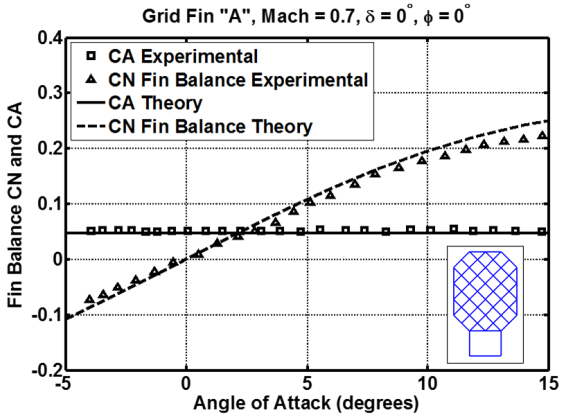

(e) Grid Fin "A", Mach 0.7, 0° Incidence Angle

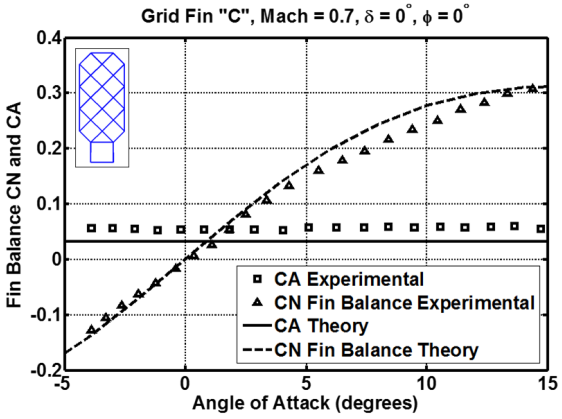

(f) Grid Fin "C", Mach 0.7, 0° Incidence Angle

Figure 4.9: Single Grid Fin, Subsonic Speeds, Not Including Fin-Body Carry-Over Loads

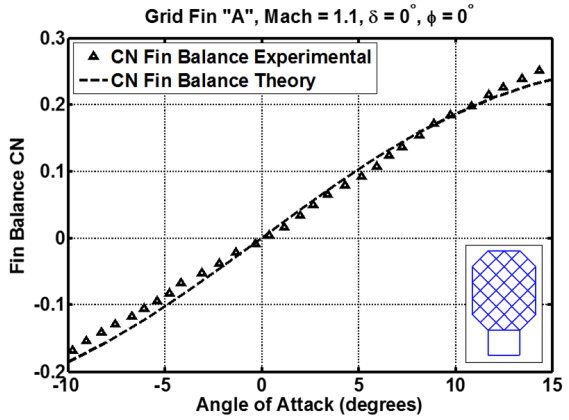

(a) Grid Fin "A", Mach 1.1, 0° Incidence Angle

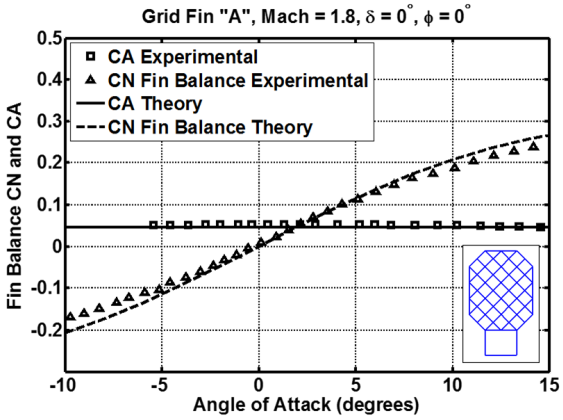

(b) Grid Fin "A", Mach 1.8, 0° Incidence Angle

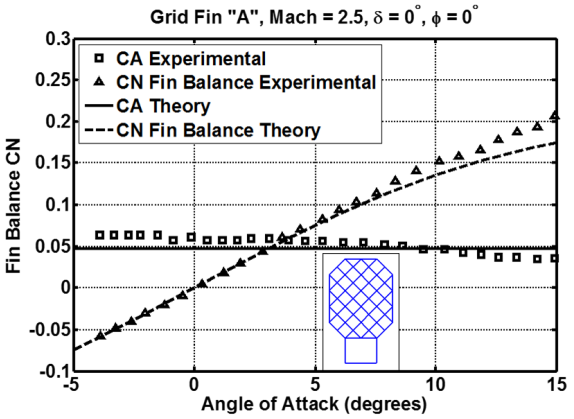

(c) Grid Fin "A", Mach 2.5, 0° Incidence Angle

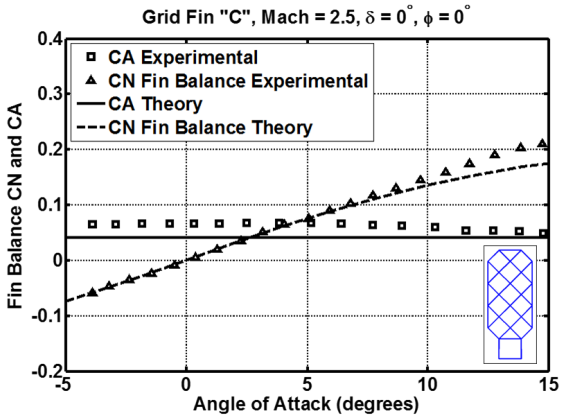

(d) Grid Fin "C", Mach 2.5, 0° Incidence Angle

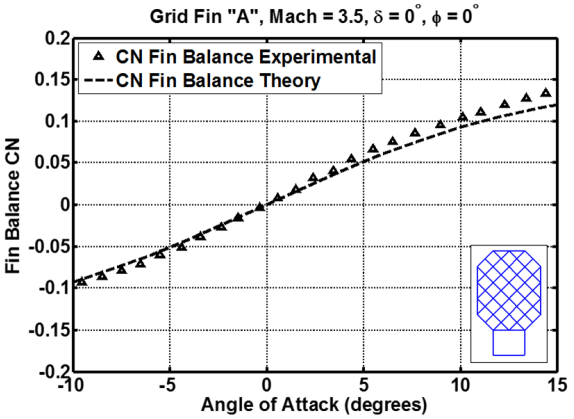

(e) Grid Fin "A", Mach 3.5, 0° Incidence Angle

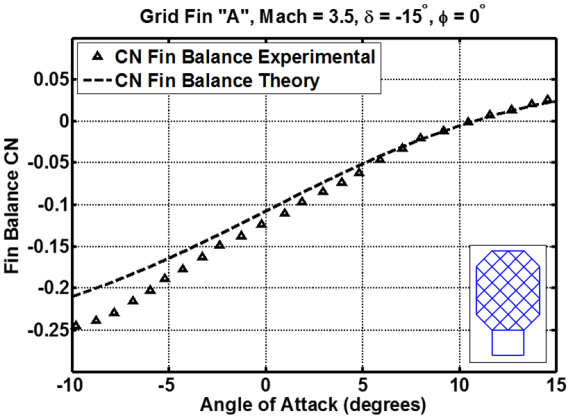

(f) Grid Fin "A", Mach 3.5, −15° Incidence Angle

Figure 4.10: Single Grid Fin, Supersonic Speeds, Not Including Fin-Body Carry-Over Loads

Chapter 5

Algorithm Description and Integration

The grid fin aerodynamic prediction programs were integrated into two different existing codes: a standalone version of AERODSN and a missile system preliminary design tool. The standalone version of AERODSN was used to conduct the validation efforts presented in the previous chapter, while the preliminary design tool was used to conduct the target strike envelope maximization problem.

5.1 Standalone AERODSN

The grid fin aerodynamic prediction algorithm was integrated with a standalone version of AERODSN for the purpose of the validation efforts shown in the previous chapter. Figure 5.1 shows a flow diagram of the program. The program begins by loading the required initial parameters from an input file that has been modified to include the information necessary for the grid fin aerodynamic prediction tool. An example of this modified input file can be seen in Appendix A. The program then begins a sweep of the specified Mach numbers, and subsequently calculates the aerodynamic coefficient derivatives for the low angle of attack region. A sweep of the specified angles of attack is then performed within the Mach number loop, where the aerodynamic coefficients for the missile configuration are calculated. This process is repeated for every angle of attack at each Mach number.

The resulting aerodynamic coefficients are then written to the output file, in either a long or short format, as specified by the user. An example of the short format output file can be seen in Appendix B. The short format shows the resulting normal force coefficient for the tail, normal force coefficient for a single grid fin, axial force coefficient for the tail, and pitching moment coefficient for each angle of attack at each Mach number. The long

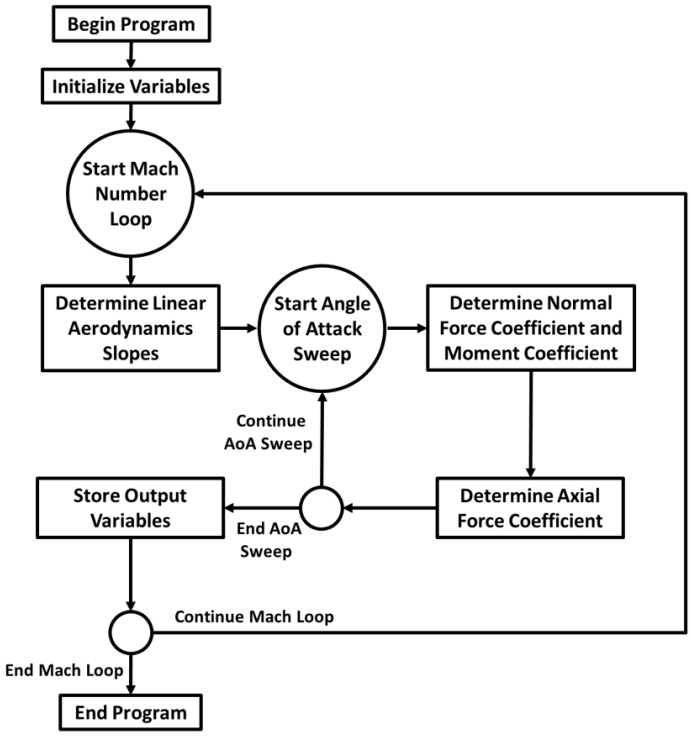

Figure 5.1: Standalone AERODSN Flow Chart

format includes each of these parameters, as well as the values for the body alone and the total configuration. An additional output file is generated (Appendix C) that defines the grid fin geometry, including the (x, y, z) coordinates of each intersection point of the grid fin and a list of each panel and the corresponding intersection points that define the endpoints of that panel.

5.2 Missile System Preliminary Design Tool

Once the grid fin aerodynamic prediction tool had been validated in conjunction with AERODSN, the program was integrated with the missile system preliminary design tool. The missile system preliminary design tool consists of a suite of optimizers that drive a full six-degree-of-freedom (6-DOF) model capable of designing single-stage missile systems to fly given trajectories or to hit specified targets. This code consists of an aerodynamics model (AERODSN), a mass properties model, and a solid propellant propulsion model. This code

has proven to be a reliable tool for aerospace design applications and has been successfully used in many previous optimization studies [20–22].

Figure 5.2 shows the flow diagram for this program. The program begins by allowing the user to select the desired optimizer and flight case and set the maximum and minimum bounds for the optimization parameters. Once this is done, the optimizer fills the initial population with feasible solutions and then begins the generational loop. The flight characteristics (mass properties, aerodynamics, and propulsion) are determined for each member of the population, and a 6-DOF fly-out is generated for each member. The fitness of each member is calculated based on the specified objective function, and a new set of solutions are then created based on the fitness of the previous population. This process is repeated until the maximum number of generations has been reached.

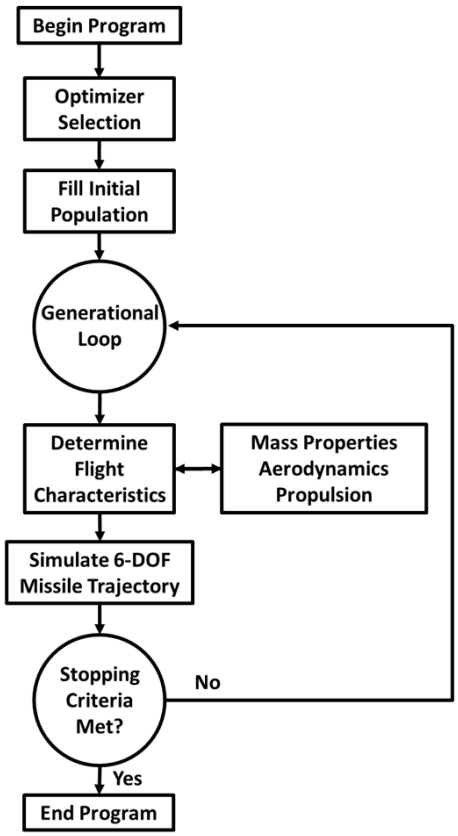

Figure 5.2: Missile System Preliminary Design Tool Flow Chart

5.2.1 Optimization

As was discussed previously, a modified ant colony optimization scheme was selected for use in this work due to its proven effectiveness at solving complex aerospace design problems [20, 21]. The ant colony is an example of a swarm intelligence algorithm, and is based on the foraging behavior of ants. The ants communicate by depositing a trail of pheromone, which allows them to determine the optimal paths to sources of food over time. The original ant colony algorithm is very effective at solving complex combinatorial problems, but is ineffective at solving complex problems in the continuous domain. The modified ant colony that is in the missile system preliminary design tool has been extended to the continuous domain by replacing the discrete pheromone links with Gaussian probability density functions. The solutions are ranked in order by their respective fitness values and a pheromone model is created, where the pheromone amount is determined by rank. The new ants are created by choosing an existing ant with a probability that is proportional to their assigned pheromone strengths. The ants sample the Gaussian distributions around each variable and combine the variables to form the new solution. The methodology behind the modified ant colony optimization algorithm is fully detailed in Reference [20].

The objective function that was used for the target strike envelope maximization problem was defined to simply be the sum of the fitness values for each individual target within the specified target grid. The fitness for each individual target was defined to be the miss distance in feet between the (x, y) location of the target and the (x, y) location where the missile actually landed, as seen by:

$$Error = \sqrt{(x_{target} - x_{actual})^2 + (y_{target} - y_{actual})^2} \tag{5.1}$$

In order to ensure that the ant colony was optimizing to increase the strike capability area rather than just minimizing the miss distance, a "maximum" miss distance of 35 feet was set so that if the missile missed a target by more than the designated distance, the fitness for

that particular target location would be set to 35. This value was chosen for the maximum miss distance because it adequately captured the zone where the target is considered to be hit while still providing room for error. If no "maximum" miss distance is set, a missile could actually miss every target in the grid and have a better fitness value than a second missile that hits 25% of the grid but misses the remaining targets by a greater amount than the first missile.

5.2.2 Flight Characteristics

The mass properties of the missile configurations are determined using a variety of empirical formulations for the different components of the missile. Included in the mass calculations are: the nose of the missile, the solid rocket motor case and liner, the warhead, the sensors and wiring, the servo actuators, the igniter, the nozzle, the wing assembly, the tail assembly, the rail, and the fuel grain. In addition to the mass of the individual components, the mass moments of inertia and the x-location of the center of gravity of the missile are calculated in this section of the code.

The aerodynamic properties for the conventional planar fin and for the cylindrical missile body are determined via AERODSN in the missile system preliminary design tool. The grid fin aerodynamic prediction algorithms were incorporated into the code so that a wide variety of grid fin designs could also be evaluated.

The propulsion properties are determined through the geometric analysis of the burning of a solid rocket motor grain. The typical grain geometry used in this code is the star grain. A parabolic nozzle design is also used in this code.

5.2.3 Program Modifications

Several modifications had to be made to the missile system preliminary design code in order to implement the target strike envelope optimization problem. The missile system preliminary design code was originally set up so that a single-stage, solid propellant missile

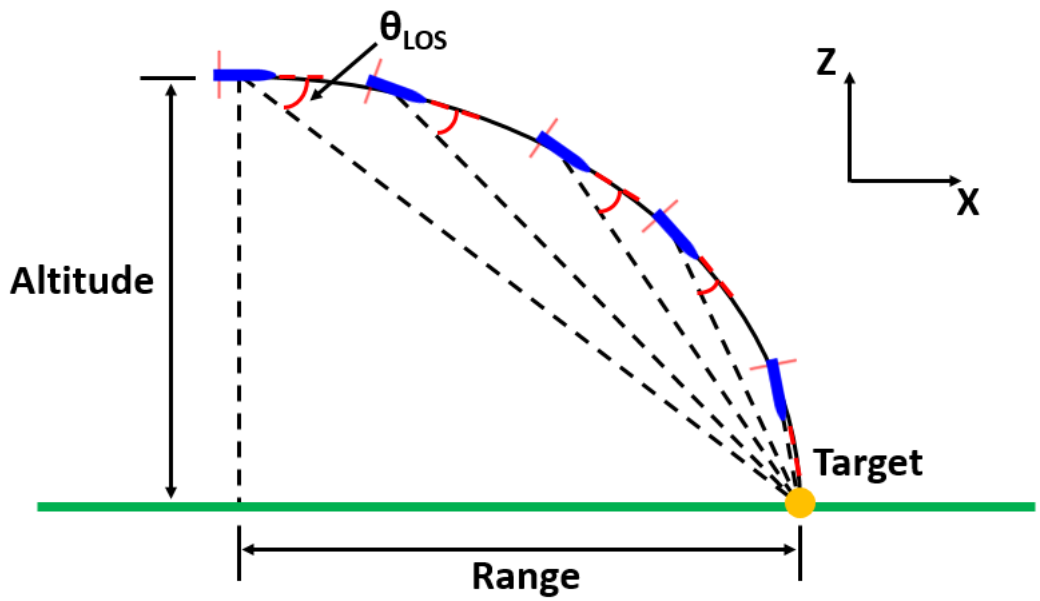

Figure 5.3: Illustration of Line-of-Sight Guidance

could launch from sea level and follow a given trajectory. For this work, all of the propulsion properties were removed, including the solid rocket motor grain modeling subroutines and the nozzle subroutines. The missile guidance algorithm was also modified to better fit the current problem. Since the purpose of the code was to match specified trajectories, the guidance algorithm was set up to follow predetermined points along the trajectory for the duration of the missile flight. For the target strike envelope maximization problem, the guidance algorithm was modified to a line-of-sight guidance system that seeks to minimize the rotation of the line-of-sight vector between the location of the missile and the location of the target. This approach is similar to proportional navigation (Pro-Nav), except that the acceleration terms are not considered in this work. Figure 5.3 shows an illustration of the line-of-sight guidance system concept for this application.

A total of ten grid fin parameters were added to the missile system preliminary design tool, which increased the total number of optimization parameters from 35 to 45. However, with the removal of the propulsion properties, the total number of parameters was reduced to 34. A total of 20 parameters were used for the planar fin optimization cases while a total of

25 parameters were used for the grid fin optimization cases. The ten grid fin parameters that were added can be seen in Figure 5.4, along with their respective maximum and minimum bounds that were used for this work. The defining geometrical parameters for the grid fin can be seen in Figure 5.5, and are:

1) Body centerline to the base of the grid fin (Y_0)

2) Body centerline to the tip of the grid fin (B_2)

3) Height of the fin support base (H_B)

4) Total height of the grid fin (H)

5) Chord length of the grid fin (C)

6) Average fin element thickness (thk)

7) Number of cells in base corner ($ibase$)

8) Number of cells in tip corner ($itip$)

9) Number of cells in span-wise direction (n_{dy})

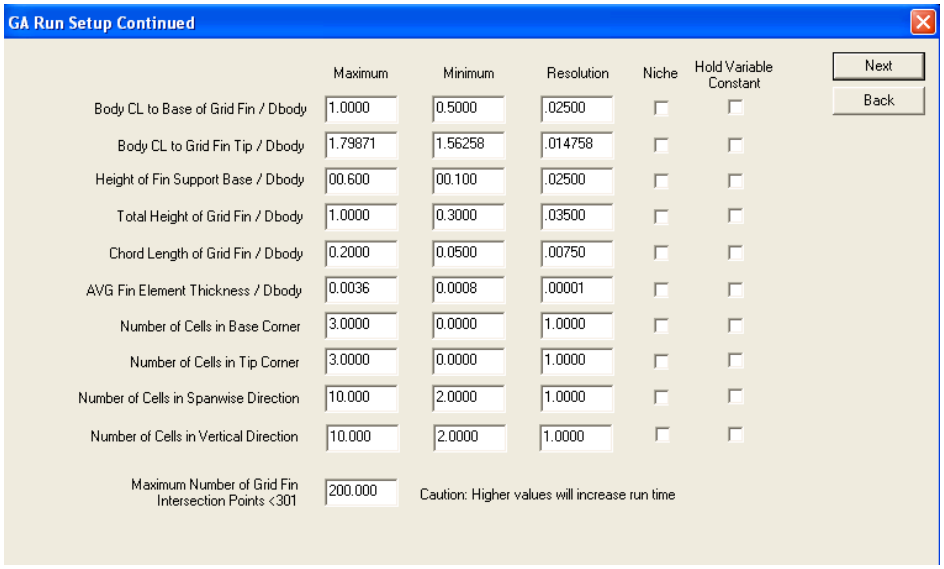

Figure 5.4: Grid Fin Parameter Optimization Constraints

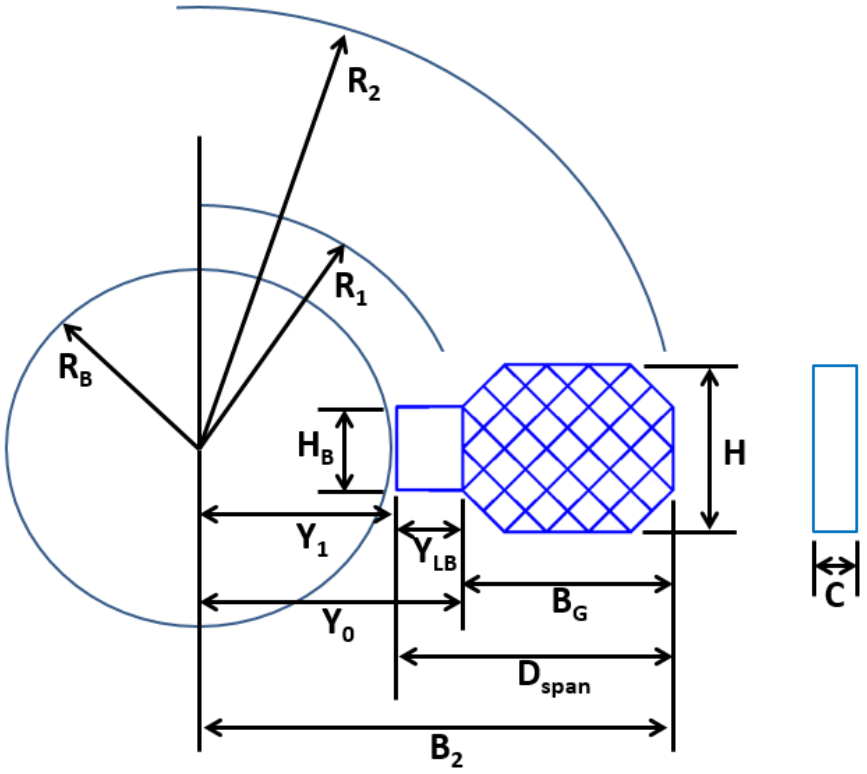

Figure 5.5: Grid Fin Parameters [12]

10) Number of cells in vertical direction (n_{dz})

Another modification made to the missile system preliminary design code was adding the ability to hold any desired optimization parameter constant. Since a direct comparison of the performance of planar fins and grid fins is desired, it is imperative to be able to hold the missile body geometry constant for each run so that any variation in performance can be attributed directly to the fins. Check boxes were added to the user interface that allow the user to mark each individual parameter that is to be held constant for that run, an example of which can be seen in Figure 5.4. If the "hold variable constant" box is selected for a parameter, the corresponding data from the most recent single run case is used for each subsequent call to the objective function.

A final modification that was required in the missile system preliminary design code was the addition of a method for the determination of the mass properties for any given grid fin geometry. In order to calculate the mass of a given grid fin geometry, a routine was

added to determine the total length of the panels of the grid fin ($L_{p_{tot}}$). This value was then multiplied by the chord length (C) and the average thickness (thk) of the elements to obtain an effective grid fin volume. Under the assumption that the grid fin is made of aluminum, the effective grid fin volume was then multiplied by the density of aluminum (ρ_{al}) in order to obtain the mass of the grid fin:

$$m_{GF} = C * thk * L_{p_{tot}} * \rho_{al} \tag{5.2}$$

The x-location of the center of gravity for the tail configuration was assumed to simply be at the half chord location of the grid fin. For the mass moment of inertia calculation, the grid fin was assumed to be a point mass, the equation for which can be seen by:

$$I_{xx} = m_{GF_i} * r_i^2 \tag{5.3}$$

where r_i is the distance from the centerline of the missile body to the half span location of the fin. The mass moments of inertia about the y and z axes are assumed to be negligible in this work.

Chapter 6

Target Strike Envelope Maximization

6.1 Problem Description

The goal of this problem is to compare the performance of an optimized missile configuration using both planar fins and grid fins as aerodynamic control devices in an effort to maximize the target strike envelope of an unpowered missile. An illustration of this problem can be seen in Figure 6.1 below. For each case, the missile was dropped from the (x, y) location of $(0, 0)$ at an altitude of 23,000 ft with a freestream (x-component) velocity of 492.8 ft/sec (336 mph). A stationary target was placed directly in front of the missile drop point at sea level at a range of 20,000 ft downstream, and a [21x21] grid of targets was then constructed around this specified central target location, as seen in Figure 6.2. The [21x21] grid size was chosen for the optimization runs in an effort to find a balance between the number of function calls required for each missile configuration that was analyzed and the

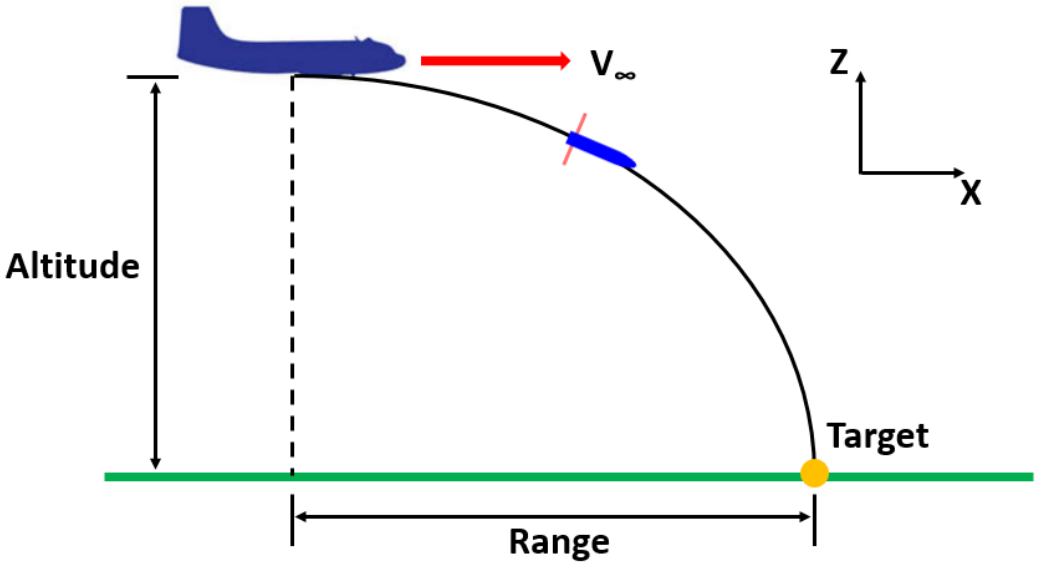

Figure 6.1: Illustration of the Missile Drop Problem

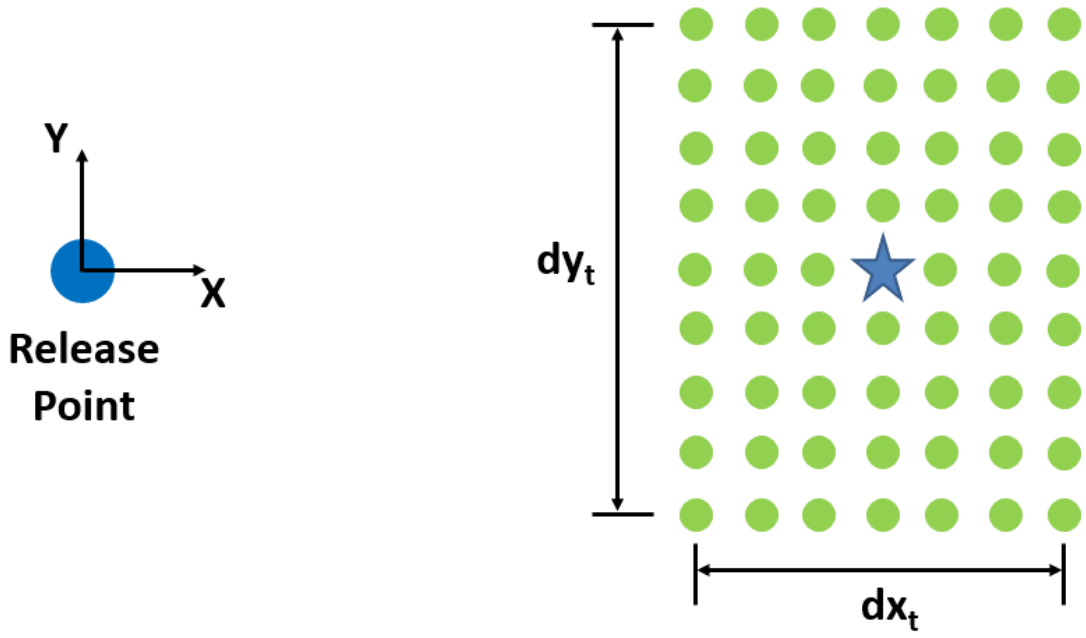

Figure 6.2: Illustration of a Target Grid for Optimization

resolution of the target grid area. Values of $dx_t = 39,000\ ft$ and $dy_t = 40,000\ ft$ were used to construct the target grid for the optimization runs so that the entire vicinity in front of the aircraft was captured. A population size of 35 members was used for each optimization run for a total of 25 generations. This resulted in the evaluation of 875 solutions at 441 different target locations each, for a total of 385,875 function calls per optimization run. A maximum fin deflection of 15° was allowed for the planar fin cases, while a maximum fin deflection of 30° was allowed for the grid fin case.

This problem was approached by first conducting the optimization of a missile configuration with grid fins so that it could strike the largest area of the target grid structure as possible. Once the optimal grid fin configuration had been found, another optimization run was conducted in which the grid fins were replaced by planar fins but the missile body parameters were held constant. In an effort to produce comparable results between the grid fin and planar fin configurations, several different constraints were applied to the problem. The first constraint was to ensure that the missile geometry had approximately the same static margin regardless of the aerodynamic control device used. This resulted in the placement

of the grid fins closer to the nose of the missile compared to the planar fins. The second constraint that was used ensured that the semi-span of the planar fin and the semi-span of the grid fin would be nearly identical. This was satisfied by using identical maximum and minimum bounds for the optimization runs for both the grid fin and planar fin cases. The third and final constraint limited the maximum hinge moment possible for the planar fin configuration. Larger hinge moments require a larger control actuator to move the fin, which requires more control power and a larger internal volume of the missile. For the purposes of this work, the maximum allowable hinge moment coefficient for the planar fin case was set to be two times the maximum hinge moment coefficient from the grid fin analysis.

6.2 Results

To show the importance of optimization in complex aerospace design problems, two unoptimized cases were run: one for a generic grid fin missile configuration and one for a generic planar fin missile configuration. The resulting target strike envelopes for these two cases can be seen in Figure 6.3 below. In the target strike envelope plots, the missile is

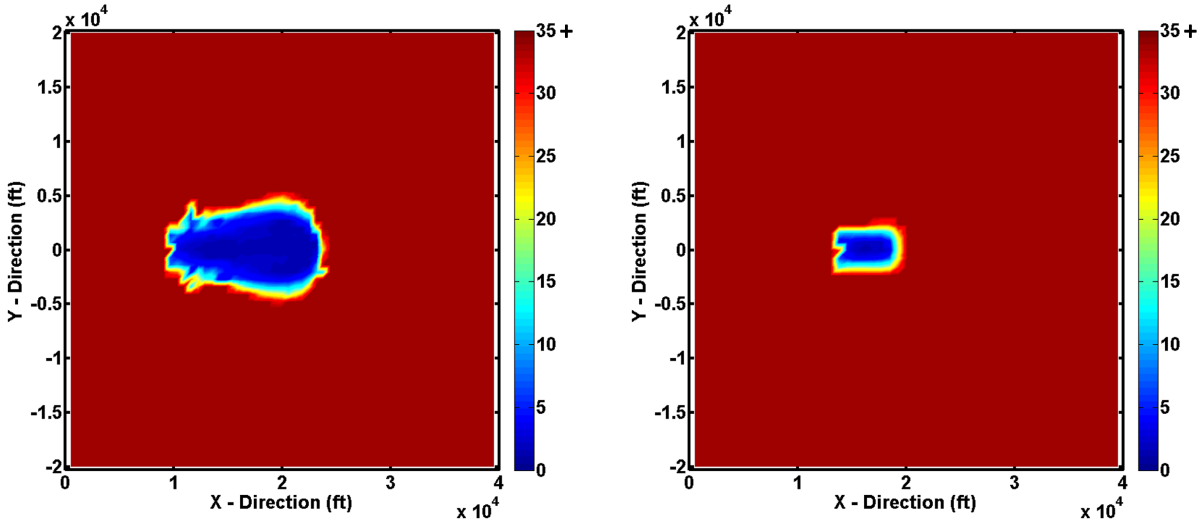

(a) Unoptimized Grid Fin Configuration (b) Unoptimized Planar Fin Configuration

Figure 6.3: Unoptimized Target Strike Envelopes

dropped from the (x, y) location of $(0, 0)$ and the color represents the miss distance in feet, as defined by the colorbar beside each plot. The total target strike area for the unoptimized grid fin case was found to be 2.60 square miles, while the total target strike area for the unoptimized planar fin case was found to be 0.51 square miles.

Figure 6.4 shows the strike area for the optimized grid fin missile configuration. It can be seen that the ant colony optimizer was able to design a missile configuration that drastically improved the target strike area, improving it from 2.60 square miles in the unoptimized case to 13.21 square miles in the optimized case.

Figure 6.5 shows the strike area for the optimized planar fin missile configuration with limited hinge moment coefficient. Similar to the grid fin case, the optimizer was able to drastically improve the performance of the planar fin missile case. The target strike area was increased from 0.51 square miles in the unoptimized case to 8.65 square miles in the optimized case. For the optimized planar fin missile configuration with unlimited hinge moment coefficient that is shown in Figure 6.6, the target strike area was found to be 19.02 square miles.

Table 6.1 shows a comparison between the optimized grid fin case, the optimized planar fin case with limited hinge moment coefficient, and the optimized planar fin case with unlimited hinge moment coefficient. It can be seen that the grid fin resulted in a substantial weight reduction, as it weighs approximately 85% less than either of the planar fin configurations. It can also be seen in Table 6.1 that the average flight time of the grid fin configuration is

Table 6.1: Optimized Missile Configuration Data

Parameter	**Grid Fin Case**	**Limited Planar Fin Case**	**Unlimited Planar Fin Case**
Target Strike Area	13.21 mi^2	8.65 mi^2	19.02 mi^2
Mass of Single Fin	20.66 lbs	139.70 lbs	115.30 lbs
Maximum Hinge Moment Coefficient	0.0862	0.1538	1.0516
Average Flight Time	59.4 sec	47.7 sec	49.5 sec

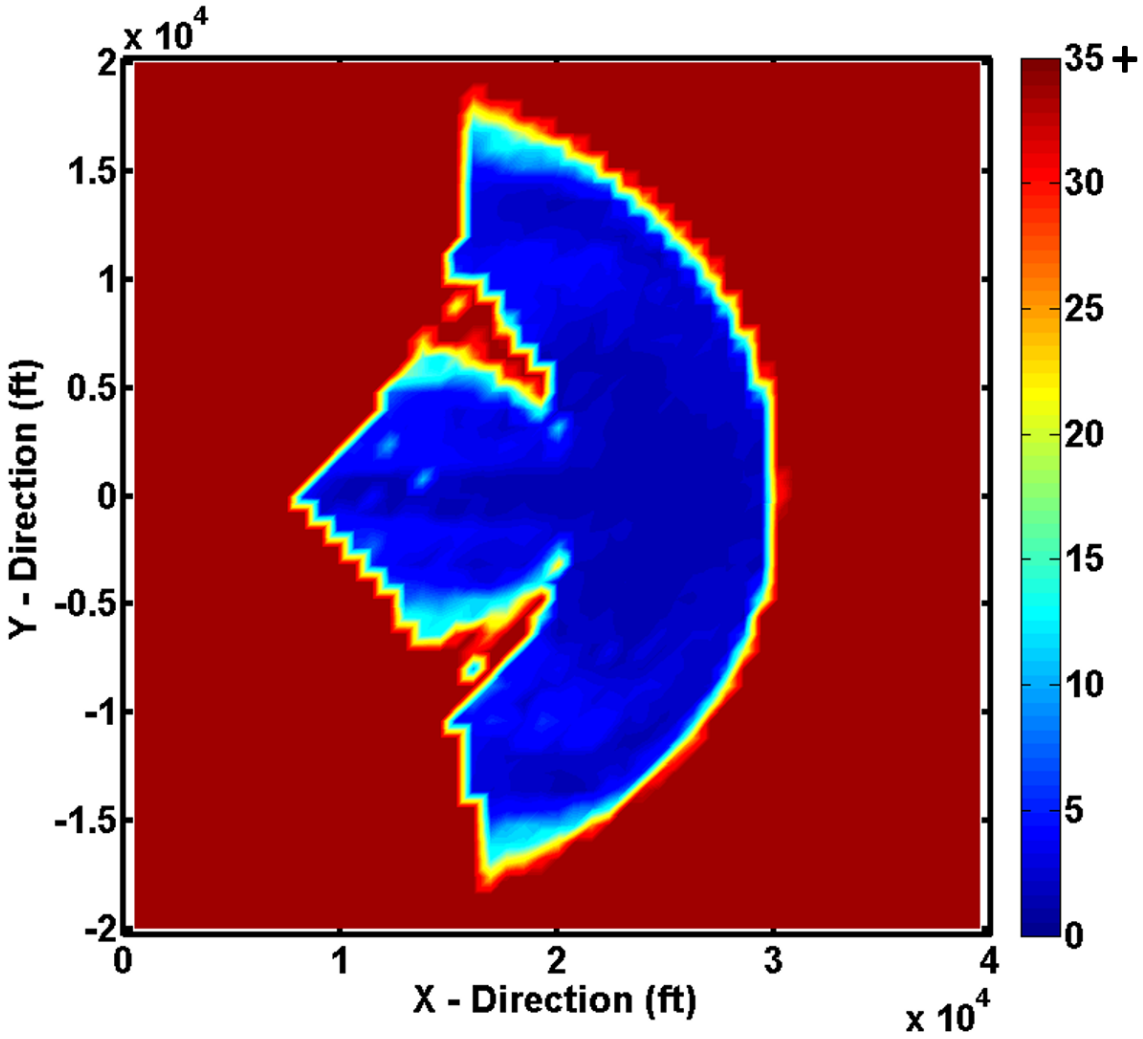

Figure 6.4: Target Strike Envelope for Optimized Grid Fin Configuration

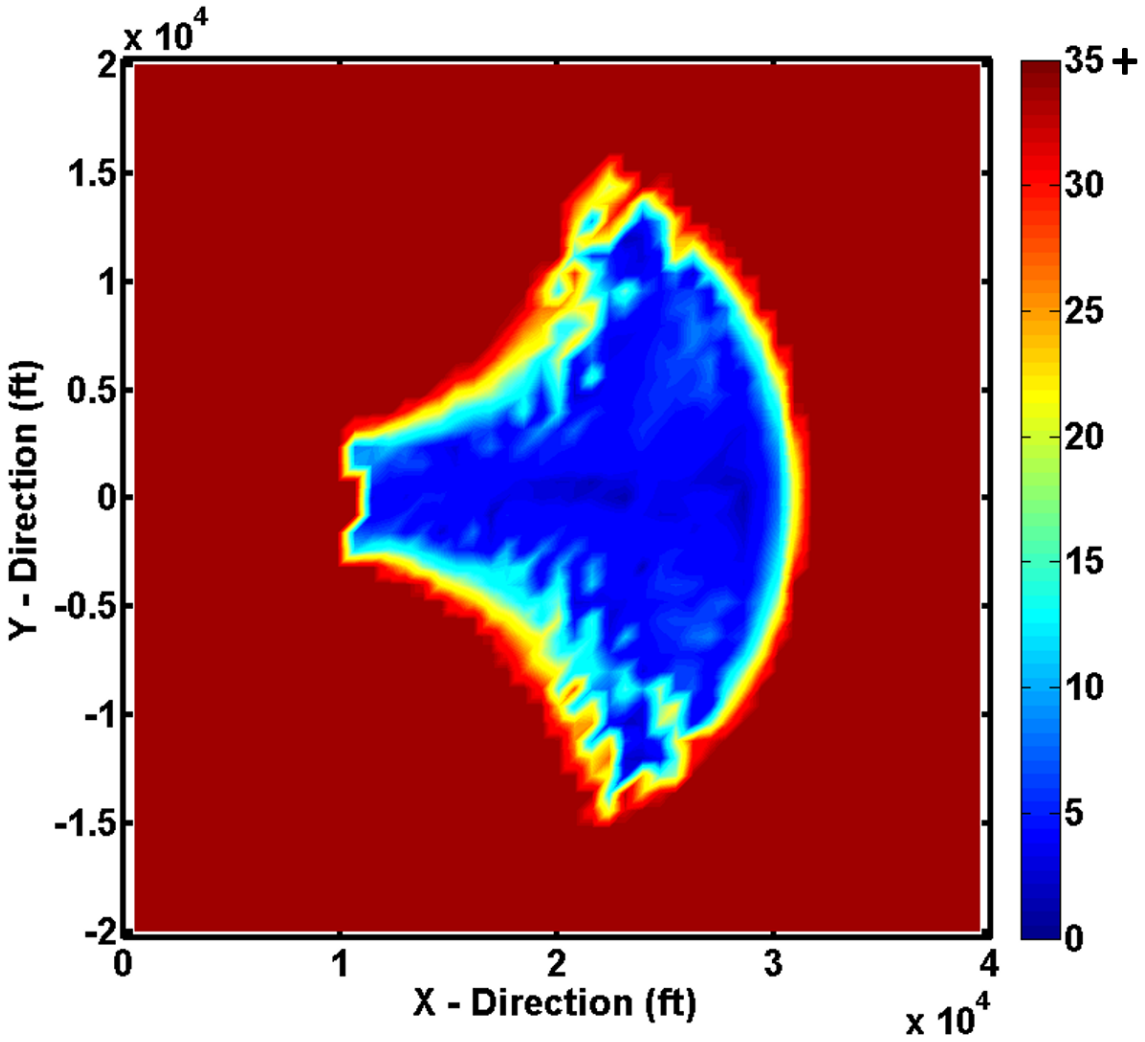

Figure 6.5: Target Strike Envelope for Optimized Planar Fin Configuration with Limited Hinge Moment

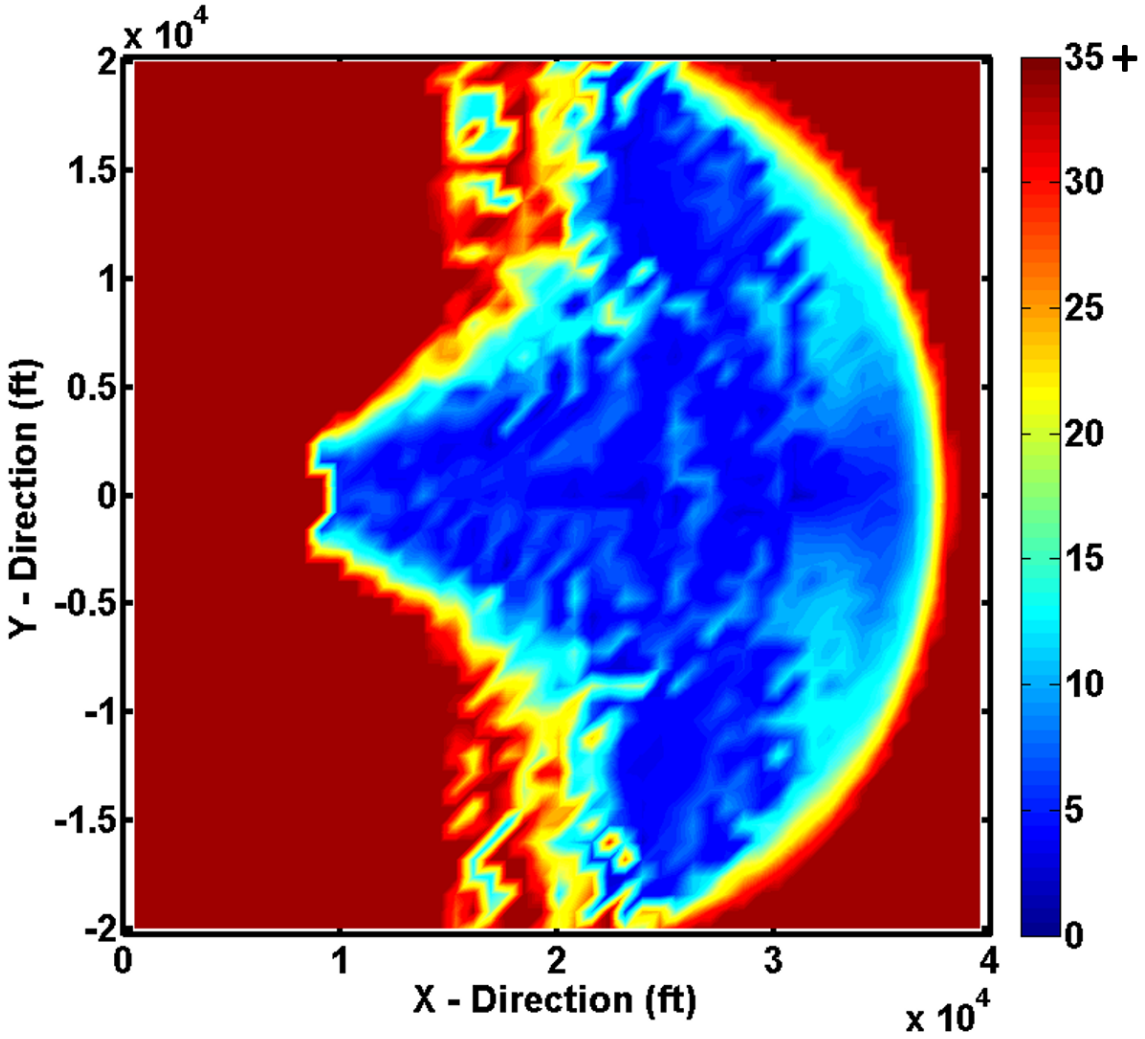

Figure 6.6: Target Strike Envelope for Optimized Planar Fin Configuration with Unlimited Hinge Moment

substantially higher than that of the planar fin cases. This is due to the higher drag that is produced by the grid fins compared to the planar fins.

A comparison of the target strike envelope of the grid fin configuration in Figure 6.4 and the planar fin configuration with limited hinge moment coefficient in Figure 6.5 shows that the missile with the grid fins is able to hit a larger range of targets than a comparable missile with planar fins. In addition to being able to hit a larger area than the planar fin configuration, the grid fin configuration is also able to hit the targets with greater precision. To show this, the average miss distance within the target strike zone was calculated for each of these cases. It was found that for the region where the missile configuration is considered to hit the target, the average miss distance for the grid fin case is 2.42 feet, while the same value for the planar fin case with limited hinge moment is 5.30 feet. This calculation was also done for the planar fin case with unlimited hinge moment coefficient in Figure 6.6, and the average miss distance was found to be 6.50 feet.

Figure 6.7 shows a comparison between the optimized grid fin geometry found in this work and a classical grid fin geometry (Grid Fin "B" from Figure 4.1). It can be seen that the cells of the optimized grid fin have been stretched in the span-wise direction so that

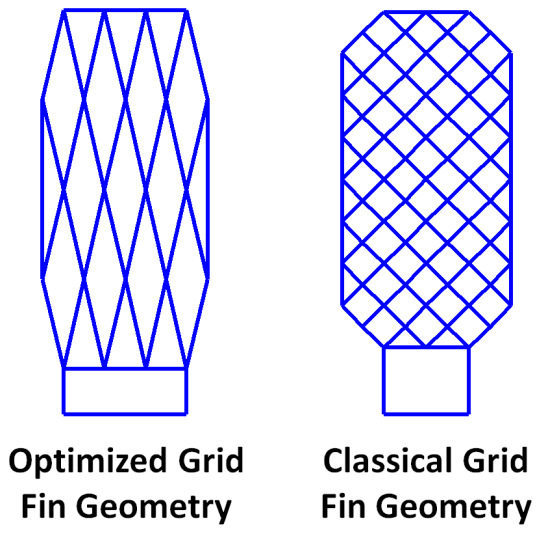

Figure 6.7: Grid Fin Comparison

the panels are not at a 45° angle. This seems to suggest that a missile configuration with classical grid fins is more effective at some finite roll angle rather than in the cruciform configuration, which is supported by the findings of Kless and Aftosmis in Reference [6]. In addition, it was found that the design parameters for the optimized grid fin geometry did not reach any of the limits that were set for the optimization runs, which indicates that the bounds used in this work were sufficient for this particular problem. The values for the optimized grid fin geometry parameters as well as their respective maximum and minimum bounds can be seen in Table 6.2. It was also noted that the initial velocity and altitude used in the target strike optimization problem resulted in strictly subsonic and transonic flow conditions for the missile configurations, meaning that the supersonic grid fin aerodynamic prediction capabilities were not used for this particular problem.

Figures 6.8 and 6.9 show the optimized missile configurations for each of these three cases. As expected, the missile body geometry is identical for all three cases. In addition, it can be seen that the grid fins are located at approximately 80% of the missile body length, while the planar fins are located closer to the tail of the missile. This placement was chosen by the optimizer to satisfy the equivalent static margin constraint discussed previously. It

Table 6.2: Optimized Grid Fin Geometry Parameters

Parameter	**Minimum Limit**	**Optimized Value**	**Maximum Limit**
Y_0/D_B	0.5	0.6276	1.0
B_2/D_B	1.56258	1.6414	1.79871
H_B/D_B	0.1	0.3489	0.6
H/D_B	0.3	0.4652	1.0
C/D_B	0.05	0.0583	0.2
thk/D_B	0.0008	0.0014	0.0036
$ibase$	0	1	3
$itip$	0	1	3
n_{dy}	2	2	10
n_{dz}	2	4	10

can also be seen that the fins in each case have approximately the same semi-span, as expected. Another interesting observation from Figure 6.8 is the optimized geometry of the planar fins in the limited and unlimited hinge moment coefficient cases. Since the missile is in completely subsonic and transonic flow, the best planar fin configuration should have an un-swept leading edge similar to that of the missile geometry for the unlimited hinge moment coefficient case. However, this design results in a hinge moment coefficient that is over twelve times higher than that of the grid fin case. In order to have lower hinge moment coefficients for the planar fin, the leading edge of the fin must be more swept, similar to the geometry found for the limited hinge moment coefficient case.

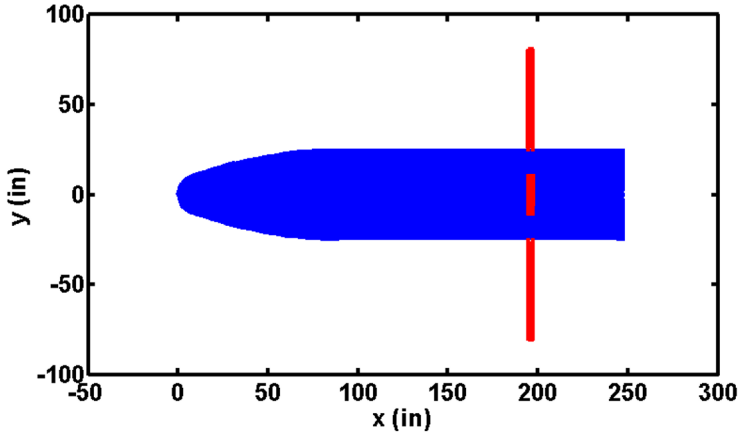

(a) Optimized Grid Fin Configuration

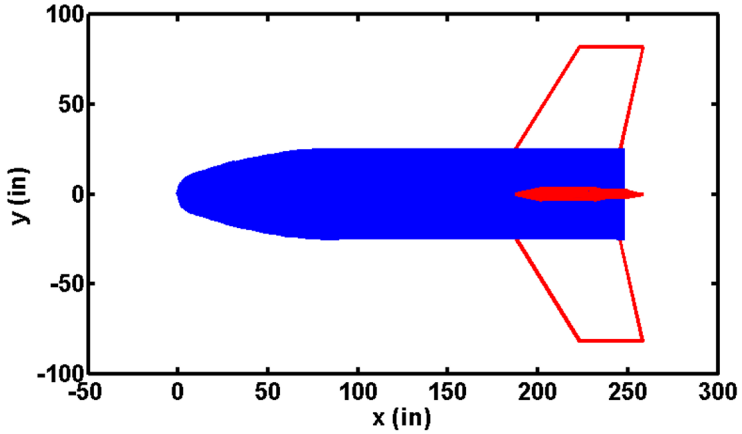

(b) Optimized Planar Fin Configuration with Limited Hinge Moment

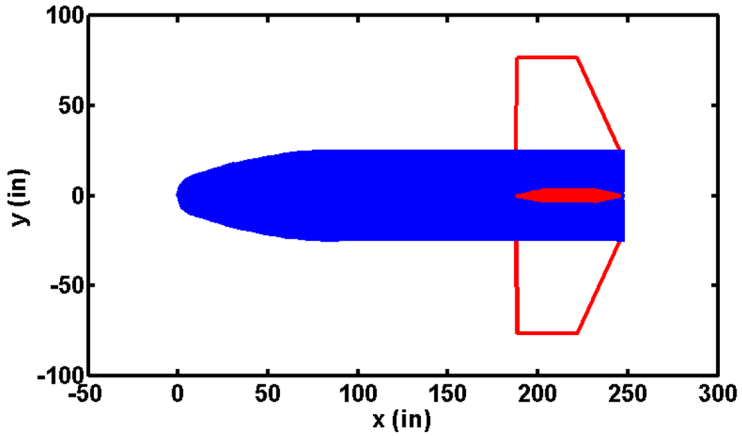

(c) Optimized Planar Fin Configuration with Unlimited Hinge Moment

Figure 6.8: Side View of Optimized Missile Geometry

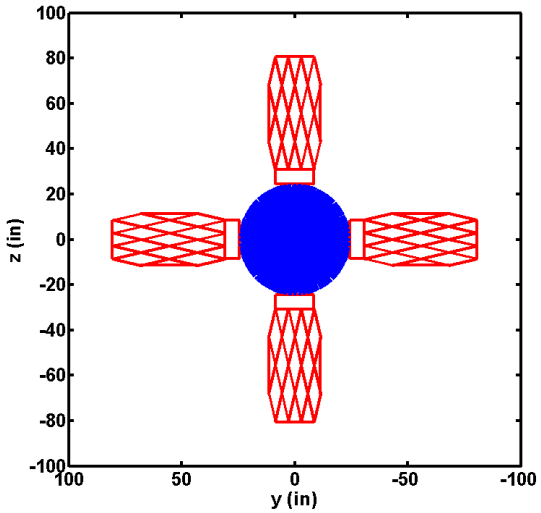

(a) Optimized Grid Fin Configuration

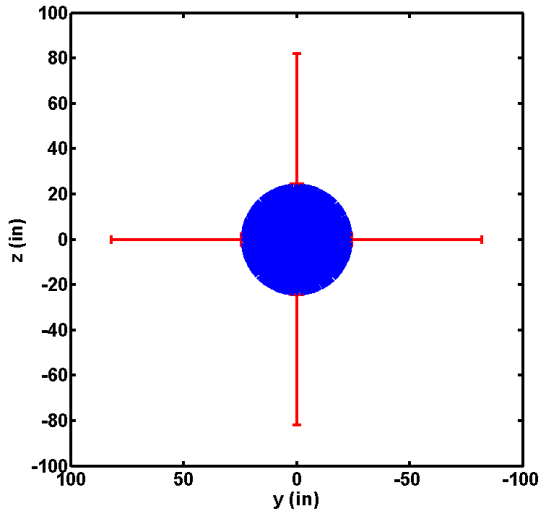

(b) Optimized Planar Fin Configuration with Limited Hinge Moment

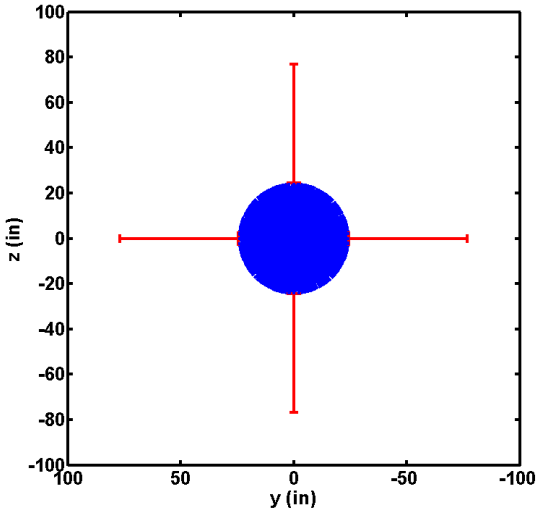

(c) Optimized Planar Fin Configuration with Unlimited Hinge Moment

Figure 6.9: Front View of Optimized Missile Geometry

Chapter 7

Conclusions and Recommendations

The subsonic, transonic, and supersonic grid fin aerodynamic prediction algorithms were successfully integrated into two different codes: a standalone version of AERODSN and a missile system preliminary design tool. The transonic grid fin aerodynamic prediction method was altered to account for the bow shock that forms in front of the grid fin at low supersonic Mach numbers, and was shown to provide accurate estimations of grid fin aerodynamics in that region. A validation of the grid fin aerodynamic prediction capability was performed using the standalone version of AERODSN for several different grid fin designs for multiple Mach numbers, configuration roll angles, and fin deflection angles. It was found that the theoretical formulations provide accurate estimations for the normal force, axial force, and pitching moment coefficients for a wide range of Mach numbers and angles of attack, and are sufficient for the prediction of grid fin aerodynamics in a preliminary-level engineering design tool. It was also shown that the imaging scheme used to model the fin-body carry-over loads is able to accurately capture the interference effects of the grid fin with the missile body.

The target strike envelope maximization problem was then conducted using the missile system preliminary design tool, where it was found that an optimized grid fin configuration is able to outperform a comparable optimized planar fin configuration. Several constraints were set in order to ensure the grid fin and planar fin cases were comparable. The first constraint ensured that the grid fin and planar fin cases both had the same fin semi-span. The second constraint ensured the planar fin missile configuration had approximately the same static margin as that of the grid fin missile configuration. The third and final constraint ensured that the planar fin could not have a maximum hinge moment coefficient that was

more than two times larger than that of the grid fin. With these constraints, the grid fin missile was able to hit a larger target area and was able to hit those targets with greater accuracy than the planar fin missile. The grid fins produced increased performance while substantially reducing the mass of the fins and the size of the control actuator required for fin control.

This research shows that, despite the high amounts of drag associated with grid fins, there are some applications where the grid fin should be seriously considered for use as a control and stability device. Additional research that could be conducted to supplement and enhance the results achieved in this work include:

1) The inclusion of wing-tail interference effects with the grid fin aerodynamics so that wings can be added to the missile configuration to see how the target strike envelope is affected by the additional lifting surfaces.

2) Investigation of different missile body geometries, including a multitude of different diameters and fineness ratios.

3) Expansion of the limits of the fin design parameters so that the optimizer is able to consider a wider range of planar fin and grid fin designs for the different missile body geometries.

4) Testing the planar fin and grid fin missile configurations at different roll angles to find the optimal orientation of the missile.

5) Performing additional wind tunnel testing on a more diverse set of grid fin geometries for further validation of the subsonic, transonic, and supersonic grid fin aerodynamic prediction codes.

6) Performing a supersonic grid fin analysis similar to the target strike problem that was done in this work.

Bibliography

[1] William D. Washington and Mark S. Miller, "Grid Fins - A New Concept for Missile Stability and Control," 31st Aerospace Sciences Meeting and Exhibit, AIAA Paper 93-0035, January 1993.

[2] William D. Washington and Mark S. Miller, "Experimental Investigations of Grid Fin Aerodynamics: A Synopsis of Nine Wind Tunnel and Three Flight Tests," AGARD Applied Vehicle Technology Panel Symposium and Meeting on Missile Aerodynamics, Paper 10, May 1998.

[3] William D. Washington, Pamela F. Booth, and Mark S. Miller, "Curvature and Leading Edge Sweep Back Effects on Grid Fin Aerodynamic Characteristics," 11th Applied Aerodynamics Conference, AIAA Paper 93-3480, August 1993.

[4] Mark S. Miller and William D. Washington, "An Experimental Investigation of Grid Fin Drag Reduction Techniques," AIAA Paper 94-1914, June 1994.

[5] G. M. Simpson and A. J. Sadler, "Lattice Controls: A Comparison with Conventional, Planar Fins," NATO Science and Technology Organization, The Applied Vehicle Technology Panel Symposium, May 1998.

[6] James E. Kless and Michael J. Aftosmis, "Analysis of Grid Fins for Launch Abort Vehicle Using a Cartesian Euler Solver," 29th AIAA Applied Aerodynamics Conference, AIAA Paper 2011-3666, June 2011.

[7] Jinsheng Cai, "Numerical Study on Choked Flow over Grid Fin Configurations," Journal of Spacecraft and Rockets, Vol. 46, No. 5, September-October 2009, pp. 949-956.

[8] Erich Schülein and Daniel Guyot, "Novel High-Performance Grid Fins for Missile Control at High Speeds: Preliminary Numerical and Exerimental Investigations," NATO Science and Technology Organization, RTO Applied Vehicle Technology Panel Symposium, May 2006.

[9] Richard W. Kretzschmar and John E. Burkhalter, "Aerodynamic Prediction Methodology for Grid Fins," U.S. Army Aviation and Missile Command, RTO Applied Vehicle Technology Panel Symposium, May 1998.

[10] John E. Burkhalter, "Characterization of Grid Fin Aerodynamics for Subsonic Flow," Final report, Contract No. DAAL03-91-C-0034, TCN Number: 95-197, Scientific Services Program, AMSMI-RD-SS-AT, Redstone Arsenal, AL, September 1995.

[11] John E. Burkhalter, "Grid Fins for Missile Applications in Supersonic Flow," 34th Aerospace Sciences Meeting and Exhibit, AIAA Paper 96-0194, January 1996.

[12] John E. Burkhalter, Roy J. Hartfield, and Todd M. Leleux,"Nonlinear Aerodynamic Analysis of Grid Fin Configurations," Journal of Aircraft, Vol. 32, No. 3, May-June 1995, pp. 547-554.

[13] Richard W. Kretzschmar, "Downwash Effects on Aft Control Surfaces for Missile Configurations in Subsonic Flow," Master's Thesis, Auburn University, August 1997.

[14] Ross A. Brooks, "An Aerodynamic Analysis of Several Grid Fin Configurations Using Vortex Lattice Method," Master's Thesis, Auburn University, August 1987.

[15] George A. Sanders and William D. Washington, "Computer Program for Estimating Stability Derivatives of Missile Configurations - Users Manual," U.S. Army Missile Command Technical Report RD-83-2, Redstone Arsenal, AL, August 1982.

[16] David B. Riddle, Roy J. Hartfield, John E. Burkhalter, and Rhonald M. Jenkins, "Design of Liquid Rocket Powered Missile Systems Using a Genetic Algorithm," Journal of Spacecraft and Rockets, Vol. 46, No. 1, January-February 2009, pp. 151-159.

[17] Douglas J. Bayley, Roy J. Hartfield, John E. Burkhalter, and Rhonald M. Jenkins, "Design Optimization of Space Launch Vehicle Using a Genetic Algorithm," Journal of Spacecraft and Rockets, Vol. 45, No. 4, July-August 2008, pp. 733-740.

[18] Roy J. Hartfield, Rhonald M. Jenkins, and John E. Burkhalter, "Ramjet Powered Missile Design Using a Genetic Algorithm," Journal of Computing and Information Science in Engineering, Vol. 7, No. 2, June 2007.

[19] Roy J. Hartfield, Rhonald M. Jenkins, and John E. Burkhalter, "Optimizing a Solid Rocket Motor Boosted Ramjet Powered Missile Using a Genetic Algorithm," Applied Mathematics and Computation, Vol. 181, No. 2, 2006, pp. 1720-1736.

[20] Zachary J. Kiyak, "Ant Colony Optimization: An Alternative Heuristic for Aerospace Design Applications," Master's Thesis, Auburn University, December 2013.

[21] Zachary J. Kiyak, Roy J. Hartfield, and Timothy W. Ledlow, "Missile Trajectory Optimization Using a Modified Ant Colony Algorithm," 2014 IEEE Aerospace Conference, AIAA Paper 2014-2185, March 2014.

[22] Timothy W. Ledlow, Zachary J. Kiyak, and Roy J. Hartfield, "Missile System Design Using a Hybrid Evolving Swarm Algorithm," 2014 IEEE Aerospace Conference, AIAA Paper 2014-2225, March 2014.

[23] Sergei M. Belotzerkovsky et al., "Wings with Internal Framework," Machine Translation, FTD-ID(RS)T-1289-86, Foreign Technology Div., February 1987.

[24] Jeffrey A. Scott, "Missile Grid Fins," http://www.aerospaceweb.org/question/weapons/q0261.shtml, February 2006.

[25] Carlo Kopp, "The Russian Philosophy of Beyond Visual Range Air Combat," Technical Report APA-TR-2008-0301, Air Power Australia, March 2008.

[26] John Reed, "USAF Providing "Options" for Dealing with Iran," http://defensetech.org/2012/03/01/usaf-providing-options-for-dealing-with-iran/, March 2012.

[27] Dynetics, "Advanced Payload Design, Development, and Integration," http://www.dynetics.com/services/intelligence/aviation-systems/advanced-payload-design-development-and-integration.

[28] John E. Burkhalter and Harris M. Frank,"Grid Fin Aerodynamics for Missile Applications in Subsonic Flow," Journal of Spacecraft and Rockets, Vol. 33, No. 1, January-February 1996, pp. 38-44.

[29] John D. Anderson, Jr., "Fundamentals of Aerodynamics," McGraw-Hill Publishing, Fifth Edition, 2011, pp. 549-598.

[30] John C. Evvard, "Use of Source Distributions for Evaluating Theoretical Aerodynamics of Thin Finite Wings at Supersonic Speeds," NACA Report 951, 1950.

[31] John E. Burkhalter, "Grid Fins in Supersonic Flow," Contractor Final report, Contract No. DAAH01-92-D-R002, DO Number NRC 0211, AMSMI-RD-SS-AT, Redstone Arsenal, AL, September 1994.

[32] Jack N. Nielsen, "Missile Aerodynamics," Nielsen Engineering & Research, Inc., 1988, pp. 112-138.

Appendices

Appendix A

Standalone AERODSN Input File

```
Optimizer Type————————————————————————
——(1=RealGA, 2=BinaryGA, 3=PSO, 4=ASO, 5=SingleRun)——
5               ;Choose Desired Optimizer                                  ...ioptimizertype
2               ;Tail Fin Flag (0=no fins, 1=planar fins, 2=grid fins)     ...itailfin
0               ;Wing Flag (0=no wing, 1=planar fin wing)                  ...iwingfin

Flight Conditions————————————————————————
1               ;Number of Freestream Mach Numbers                         ...NFMA
0.5             ;Table of Freestream Mach Numbers                          ...TFMA
0.0             ;Altitude for Each Mach Number (ft)                        ...TALT

Missile Body————————————————————————
1               ;Number of Freestream Mach Numbers                         ...NFMA
0.4167          ;Reference Length (ft)                                     ...DREF
0.136354        ;Reference Area (ft^2)                                     ...AREF
1.25            ;Nose Length (ft)                                          ...XLN
4.333           ;Total body Length (ft)                                    ...XL
0.2083          ;Radius Body at Wing (ft)                                  ...RBW
0.2083          ;Radius Body at Tail (ft)                                  ...RBT
1.75            ;Nose to Wing Hinge Line (ft)                              ...THINGW
3.833           ;Nose to Tail Hinge Line (ft)                              ...THINGT
1               ;Nose Type 1-Ogive 2-Cone                                  ...NOSE
4               ;Total Number of Fins on Tail                              ...numbfinsT
2               ;Total Number of Fins on Wing                              ...numbfinsW
0               ;Add Boattail (0=NO, 1=YES)                                ...NBTL
1.0             ;Boattail Diameter/Cylinder Diameter                       ...DBOD
0.001           ;Boattail Length/Cylinder Diameter                         ...XLBOD

Grid Fin Parameters———(G12)————————————
0.28025         ;Body CL to Base of Grid fin (ft)                          ...yzro
0.280167        ;Min Radius for Grid Points (ft)                           ...r1
0.508583        ;Body CL to Grid fin Tip (ft)                              ...b2
0.09            ;Height of Fin Support Base (ft)                           ...hb
0.07192         ;Span of Fin support Base (ft)                             ...ylb
0.18167         ;Total Height of Fin (ft)                                  ...h
0.032           ;Chord Length of Fin (ft)                                  ...chord
```

```
0.000667        ;Average Fin Element Thickness (ft)                    ...thk
2               ;Fin Base corner type; No Cells in Base Corner         ...ibase
2               ;Fin Tip corner type; No Cells in Tip corner           ...itip
5.0             ;No Cells in Spanwise Direction                        ...ndy
4.0             ;No Cells in Vertical Direction                        ...ndz
1               ;No vortices per element chordwise                     ...nvc
1               ;No vortices per element spanwise                      ...nvs
00.00           ;Roll Angle for Configuration                          ...phii
1, 90.0, 0.0    ;Fin No, Angle Phi, Incidence Angle                    ...ifin,phi,delta
2, 0.0, 0.0     ;Fin No, Angle Phi, Incidence Angle                    ...ifin,phi,delta
3, 270.0, 0.0   ;Fin No, Angle Phi, Incidence Angle                    ...ifin,phi,delta
4, 180.0, 0.0   ;Fin No, Angle Phi, Incidence Angle                    ...ifin,phi,delta
16              ;No Alphas (Angles Listed Below)                       ...nalpa
-10.0,-8.0,-6.0,-4.0,-2.0,0.0,2.0,4.0,6.0,8.0,10.0,12.0,14.0,16.0,18.0,20.0

Planar Tail Fin Parameters----------
2.0             ;Tail Exposed Semispan (B/2)                           ...TBOT
4.00            ;Tail Root Chord (Croot)                               ...TCRT
0.5             ;Tail Taper Ratio (Ctip/Croot)                         ...TTRT
0.0             ;Tail Trailing Edge Sweep Angle (deg)                  ...TSWTET
20.0            ;Tail Position (Measured from nose)                    ...TXTAIL
0.0             ;Tail Deflection (deg)                                 ...TDELT

Wing Parameters----------
0.001           ;Wing Exposed Semispan (B/2)                           ...TBOW
0.001           ;Wing Root Chord (Croot)                               ...TCRW
1.0             ;Wing Taper Ratio (Ctip/Croot)                         ...TTRW
0.0             ;Wing Trailing Edge Sweep Angle (deg)                  ...TSWTEW
5.0             ;Wing Station (Measured from nose)                     ...TXWING
0.0             ;Wing Deflection (deg)                                 ...TDELW

AERODSN Inputs----------
1               ;Wing Station Flag                                     ...NWPOS
1               ;Tail Station Flag                                     ...NTPOS
1               ;Use NACA Report 1253                                  ...MCDVT
3               ;Alpha and Trim Output                                 ...NOUT
1               ;Initial Run Number                                    ...NRUN

Miscellaneous Inputs----------
0.5             ;Mach Number for XCG                                   ...TMF
5.1996          ;C.o.G. (calibers from nose)                           ...TXCG
6000.0          ;Weight (lbs)                                          ...TWEIGH
6               ;No Iteration Loops < 10                               ...nloops
1               ;Short Output (=1) or Long Output (=0)                 ...ishortoutput
```

Appendix B

Standalone AERODSN Output File

ALP	CNT	CNTbal	CDT	CMCG
-10.0000	-0.76221	-0.29774	0.45077	1.49997
-8.00000	-0.67739	-0.26119	0.45077	1.46332
-6.00000	-0.55770	-0.21148	0.45077	1.29273
-4.00000	-0.40153	-0.14936	0.45077	0.97893
-2.00000	-0.21171	-0.07741	0.45077	0.53225
0.00000	0.00000	0.00000	0.45077	0.00000
2.00000	0.21171	0.07741	0.45077	-0.53225
4.00000	0.40153	0.14936	0.45077	-0.97893
6.00000	0.55770	0.21148	0.45077	-1.29273
8.00000	0.67739	0.26119	0.45077	-1.46332
10.0000	0.76221	0.29774	0.45077	-1.49997
12.0000	0.81590	0.32182	0.45077	-1.42802
14.0000	0.84327	0.33502	0.45077	-1.26682
16.0000	0.84945	0.33930	0.45077	-1.04070
18.0000	0.83929	0.33661	0.45077	-0.77262
20.0000	0.81702	0.32870	0.45077	-0.48718

Appendix C

Grid Fin Geometry Output File

Panel Coordinates

Point Number	x	y	z
1	45.8040	2.2104	0.5352
2	45.8040	2.2104	-0.5352
3	45.8040	3.1584	0.5250
4	45.8040	3.1584	-0.5250
5	45.8040	3.6834	1.0500
6	45.8040	3.6834	0.0000
7	45.8040	3.6834	-1.0500
8	45.8040	4.2084	0.5250
9	45.8040	4.2084	-0.5250
10	45.8040	4.7334	1.0500
11	45.8040	4.7334	0.0000
12	45.8040	4.7334	-1.0500
13	45.8040	5.2584	0.5250
14	45.8040	5.2584	-0.5250
15	45.8040	5.7834	1.0500
16	45.8040	5.7834	0.0000
17	45.8040	5.7834	-1.0500
18	45.8040	6.3084	0.5250
19	45.8040	6.3084	-0.5250
20	45.8040	6.8334	1.0500
21	45.8040	6.8334	0.0000
22	45.8040	6.8334	-1.0500
23	45.8040	7.3584	0.5250
24	45.8040	7.3584	-0.5250

Panel Connect Points for 43 Panels

Panel Number	Inboard Point	Outboard Point
1	1	2
2	1	3
3	2	4
4	3	4
5	3	5
6	3	6

7	4	6
8	4	7
9	5	8
10	5	10
11	6	8
12	6	9
13	7	9
14	7	12
15	8	10
16	8	11
17	9	11
18	9	12
19	10	13
20	10	15
21	11	13
22	11	14
23	12	14
24	12	17
25	13	15
26	13	16
27	14	16
28	14	17
29	15	18
30	15	20
31	16	18
32	16	19
33	17	19
34	17	22
35	18	20
36	18	21
37	19	21
38	19	22
39	20	23
40	21	23
41	21	24
42	22	24
43	23	24
Chord Length	0.3840	

Appendix D

Best Fitness vs. Number of Function Calls Output File

Plot	Best Fitness vs. Number of Function Calls
1	12781.1409493058
22	2158.93799077375
37	1846.62774054338
45	1296.37822732603
121	776.518078551530
157	486.499008026406
241	427.540782168719
276	274.335273449429
344	166.334585000184
379	84.9423373596193
414	60.7299095486573
519	57.4228834720672
594	24.2771689080268
728	6.19279599233190

Appendix E

Best Fit Member Output File

```
0.418049484491      ; - 1 rnose/rbody
1.821997761726      ; - 2 lnose/dbody
0.000000000000      ; - 3 fuel type
0.000000000000      ; - 4 star outer R rpvar=(rp+f)/rbody
0.000000000000      ; - 5 star inner ratio=ri/rp
0.000000000000      ; - 6 number of star pts
0.000000000000      ; - 7 fillet radius ratio=f/rp
0.000000000000      ; - 8 eps (star PI*eps/N) width
0.000000000000      ; - 9 star point angle deg
0.000000000000      ; - 10 fractional noz len f/ro
0.000000000000      ; - 11 Dia throat/Dbody=Dstar/Dbody
5.500650882721      ; - 12 Fineness ratio Lbody/Dbody
1.067551493645      ; - 13 dia of stage1 meters
0.000572043238      ; - 14 wing semispan/dbody
0.000541782822      ; - 15 wing root chord = crw/dbody
0.852307617664      ; - 16 taper ratio = ctw/crw
40.037799835205     ; - 17 wing LE sweep angle deg
0.406034529209      ; - 18 xLE xLEw/lbody
1.289271235466      ; - 19 tail semispan/dbody
1.016451358795      ; - 20 tail root chord = crt/dbody
0.595359325409      ; - 21 tail taper ratio = ctt/crt
0.914866983891      ; - 22 LE sweep angle deg
0.990155518055      ; - 23 xTEt xTEt/lbody
1.484631061554      ; - 24 auto pilot delay time sec
0.169458851218      ; - 25 initial launch angle deg
2.652890920639      ; - 26 gainp1 - pitch multiplier gain
3.816827058792      ; - 27 gainy1 - yaw multiplier gain
0.000000000000      ; - 28 noz exit dia/dbody
-1.100889801979     ; - 29 initial pitch cmd angle (deg)
3.564826965332      ; - 30 gainp2 - angle dif gain in pitch
2160.249023437500   ; - 31 warmas - warhead mass
0.928660809994      ; - 32 time step to actuate nozzle (sec)
0.106755934656      ; - 33 gainy2 - angle dif gain in yaw
0.471196562052      ; - 34 initial launch direction (deg)
0.000751175161      ; - 35 initial pitch cmd angle (deg)
0.633140861988      ; - 36 body CL to base of GF/Dbody
```

```
2.755671262741          ; - 37 body CL to GF tip/Dbody
0.413074821234          ; - 38 height of GF support base/Dbody
0.456009268761          ; - 39 total height of GF/Dbody
0.155281305313          ; - 40 chord length of GF/Dbody
0.001375171472          ; - 41 AVG GF element thickness/Dbody
2.746897697449          ; - 42 number of cells in GF base corner
1.935090422630          ; - 43 number of cells in GF tip corner
7.035898685455          ; - 44 num. cells in spanwise dir of GF
9.773223876953          ; - 45 num. cells in vertical dir of GF
```

Appendix F

Target Fitness Output File

Target X Location	Target Y Location	Miss Distance
15000.0000000000	-5000.00000000000	8.39709064924577
17500.0000000000	-5000.00000000000	17.6984989344853
20000.0000000000	-5000.00000000000	0.55546873193927
22500.0000000000	-5000.00000000000	0.46364226301213
25000.0000000000	-5000.00000000000	0.48115083424448
15000.0000000000	-2500.00000000000	2.81273243773808
17500.0000000000	-2500.00000000000	1.94617933155096
20000.0000000000	-2500.00000000000	10.6224313763366
22500.0000000000	-2500.00000000000	0.71977713125060
25000.0000000000	-2500.00000000000	0.29650714325997
15000.0000000000	0.00000000000000	0.54816644488302
17500.0000000000	0.00000000000000	0.28955690189483
20000.0000000000	0.00000000000000	0.09350200932901
22500.0000000000	0.00000000000000	0.04924306392080
25000.0000000000	0.00000000000000	0.19718661372204
15000.0000000000	2500.00000000000	1.88601935151651
17500.0000000000	2500.00000000000	1.62695897281247
20000.0000000000	2500.00000000000	5.78243053170833
22500.0000000000	2500.00000000000	0.55620057990438
25000.0000000000	2500.00000000000	0.19905981613441
15000.0000000000	5000.00000000000	5.89321404691875
17500.0000000000	5000.00000000000	8.68805009978391
20000.0000000000	5000.00000000000	0.63275712621600
22500.0000000000	5000.00000000000	0.51010608066574
25000.0000000000	5000.00000000000	0.41572819670044

5 5